Journal of Energy Storage 154 (2026) 121209

Contents lists available at ScienceDirect

Journal of Energy Storage

journal homepage: www.elsevier.com/locate/est

Research papers

Li-decorated Ti_4ZnO_9 monolayer for high-capacity hydrogen storage

Gokhan Surucu [a,*], Cagri Karadeniz [b], Ozge Surucu [c], Aysenur Gencer [d]

[a] Department of Energy Systems Engineering, Faculty of Technology, Gazi University, 06500, Ankara, Türkiye
[b] Graduate School of Natural and Applied Sciences, Gazi University, 06500, Ankara, Türkiye
[c] Department of Energy Systems Engineering, Faculty of Engineering and Natural Sciences, Ankara Yildirim Beyazit University, 06010, Ankara, Türkiye
[d] Department of Physics, K. O. Faculty of Science, Karamanoglu Mehmetbey University, 70200, Karaman, Türkiye

ARTICLE INFO

Keywords:
Hydrogen storage
Density functional theory
Li decoration
Ti_4ZnO_9 material

ABSTRACT

In this study, a novel two-dimensional (2D) Ti_4ZnO_9 monolayer is proposed for hydrogen storage applications, and its potential, as enhanced by Lithium (Li) decoration, was systematically investigated using first-principles density functional theory (DFT). The pristine Ti_4ZnO_9 monolayer was confirmed to be an insulator possessing robust thermodynamic, mechanical, and dynamic stability, indicating its experimental feasibility. The most energetically favorable Li decoration site (Li1) was identified, and this decoration was found to induce metallicity in the system. A significant charge transfer from the Li atoms to the Ti_4ZnO_9 surface facilitates a physisorption-based H_2 adsorption mechanism. The hydrogen storage performance of the two-sided Li1-decorated Ti_4ZnO_9 system was found to be exceptional, with a maximum gravimetric storage capacity of 6.05 wt% being achieved. This value significantly surpasses the 5.5 wt% target set by the US Department of Energy (DOE) for 2025. A critical analysis of the adsorption energies revealed the material's versatility: while the maximum 6.05 wt% capacity corresponds to a low adsorption energy (0.11 eV/H_2) suitable for cryogenic storage (85.24 K), a high capacity of 4.27 wt% is also offered. This latter capacity is achieved with an ideal adsorption energy (0.41 eV/H_2), enabling reversible storage at a near-ambient desorption temperature of 302.43 K. Based on these findings, Li-decorated Ti_4ZnO_9 is established as a highly promising and flexible platform for next-generation solid-state hydrogen storage.

1. Introduction

Hydrogen is considered a leading candidate for clean energy applications due to its high gravimetric energy density, abundance, and zero carbon emissions at the point of use [1]. However, the safe, efficient, and reversible storage of hydrogen remains a major challenge for its widespread adoption in transportation, stationary energy systems, and portable devices [2,3]. Among the available storage strategies, solid-state hydrogen storage offers significant advantages over compressed and cryogenic hydrogen, including improved safety and the potential for higher volumetric densities under moderate conditions [4,5].

A wide variety of materials have been investigated for solid-state hydrogen storage, such as metal hydrides, complex hydrides, carbon-based materials, and metal–organic frameworks (MOFs) [6–9]. While some systems exhibit high storage capacities, many suffer from slow kinetics, high desorption temperatures, or structural instability during cycling [10]. Titanium-based oxides have attracted attention due to their chemical stability, tunable surface chemistry, and ability to interact with hydrogen via physisorption, chemisorption, or Kubas-type interactions [11,12]. For example, chemically reducible micro- and mesoporous Ti oxides with controlled pore sizes (12–26 Å) have demonstrated reversible hydrogen uptake up to 5.63 wt% at 77 K and 100 atm, with binding enthalpies (~4.2–8.1 kJ/mol) in the range predicted for near-ambient temperature operation [13].

Zinc oxide systems have also shown promising hydrogen adsorption characteristics. Pure ZnO nanowires achieve 2.57 wt% uptake at room temperature, while Mg-doped ZnO nanowires reach 2.79 wt% under similar conditions [14]. The hydrogen absorption process is primarily chemisorptive, involving O—H bond formation and desorption in the 100–250 °C range. Structural factors such as nanorod spacing significantly affect adsorption by enabling inter-surface hydrogen accommodation and charge transfer from H_2 to the oxide surface [15,16].

Titanium- and zinc-based oxides have shown promising hydrogen adsorption properties due to their tunable electronic structures and mixed bonding characteristics. In particular, Ti—Zn oxide composites combine the stability of TiO_2 with the charge-transfer properties of ZnO,

* Corresponding author.
E-mail address: gokhansurucu@gazi.edu.tr (G. Surucu).

https://doi.org/10.1016/j.est.2026.121209
Received 6 November 2025; Received in revised form 20 January 2026; Accepted 17 February 2026
2352-152X/© 2026 Elsevier Ltd. All rights are reserved, including those for text and data mining, AI training, and similar technologies.

forming robust heterostructures suitable for hydrogen interaction [17–21]. Motivated by these features, this study proposes a new Ti_4ZnO_9 two-dimensional composition, hypothesized to offer dual-metal binding sites and enhanced hydrogen affinity. To further improve adsorption performance, surface modification with light alkali metals, particularly lithium (Li), is introduced to increase active sites and optimize binding energies [22–26]. Given Ti_4ZnO_9's structural stability and potential dual-metal binding sites, Li decoration is expected to significantly improve its hydrogen storage characteristics. Clustering is an imperative consideration in the context of metal decoration. As demonstrated by Mishra et al. [27], the study conducted on polycrystalline carbon nanotubes determined that the prevention of Ti clustering can be achieved by means of heteroatom doping. In another study, Kerdsombut et al. [28] demonstrated that clustering does not occur in Sc, Ti and V decoration for C_5N monolayers, due to strong bonding energies and high diffusion barriers. The results of the present study indicate that ab-initio molecular dynamics calculation does not result in the formation of a cluster for the Li decorated Ti_4ZnO_9.

Building on these considerations, this study conducts a first-principles investigation of Li-decorated Ti_4ZnO_9 for hydrogen storage applications. The structural, electronic, and adsorption properties of both pristine and Li-modified surfaces are examined to identify the most stable decoration sites and evaluate their hydrogen adsorption behavior. The results provide fundamental insights into the stability, binding mechanisms, and storage potential of the system, highlighting Li-decorated Ti_4ZnO_9 as a promising platform for efficient solid-state hydrogen storage.

2. Computational details

The hydrogen storage properties of Li-decorated Ti_4ZnO_9 material was investigated using the Vienna Ab-initio Simulation Package (VASP) [29,30] based on the density functional theory. The electron-electron interactions were considered using the Perdew-Burke-Ernzerhof (PBE) functional [31] within the Generalized Gradient Approximation (GGA) while the Projected Augmented Wave (PAW) method [32,33] was employed for the electron-ion interactions. The calculations were performed using an energy cut off taken as 530 eV and a gamma centered grid [34] of $4 \times 4 \times 1$ k-points. The energy and force convergence criteria were set to 10^{-7} eV per unit cell and 10^{-6} eV/Å, respectively. The finite displacement method was employed for the phonon dispersion curves calculations using the Phonopy package [35,36]. The van der Waals corrections were included using DFT-D3 correction [37]. Furthermore, a vacuum space as 15 Å was taken to prevent the interactions between the layers. The energy-strain method was used to determine the elastic constants of Ti_4ZnO_9 material using ELASTOOL program [38,39]. The H_2 positions were determined using the Cap Like Initial Conditions (CLICH) algorithm [40]. For the algorithm, the bond length of H_2 was taken as 0.74 Å which is the experimental value [41]. θ, z_{max}, and r_{up} were taken as 45°, 3 Å, and 1 Å for $n = 1$–6, respectively. In the systems under consideration for the n≥7, the radial distance between the H_2 molecules was fixed at h = 1.3 Å, as opposed to the fixed radius (r_{up}). The crystal structures and the electronic band structures were visualized using the VESTA program [42] and the Sumo tools [43], respectively. In order to execute the Bader partial charge calculations, the VASP was utilized, and the analysis was conducted employing an algorithm which was developed by the Henkelman group [44] which is based on a suggestion put forward by Bader [45]. Furthermore, ab initio molecular dynamics calculations were performed at zero pressure and 300 K temperature using dynamic variables such as atomic positions and lattice parameters. The Langevin thermostat [46,47] was utilized, with values of 10 ps^{-1}, 10 ps^{-1}, 5 ps^{-1}, 3 ps^{-1}, 3 ps^{-1}, and 4 ps^{-1} being employed for Ti, Zn, O, Li, H atoms, and lattice friction, respectively. The ion motion equations were integrated with a 1 fs time step using the Verlet algorithm. As AIMD calculations are computationally expensive and time-consuming, the machine learning force field (MLFF) implemented in VASP [48,49] was utilized. The machine learning potential energy surface was defined by descriptors based on the Gaussian representation of atomic distributions [49,50]. Furthermore, target properties, including energy, forces, and strain tensor components, were obtained using Bayesian linear regression [48,51], which provides reliable predictions.

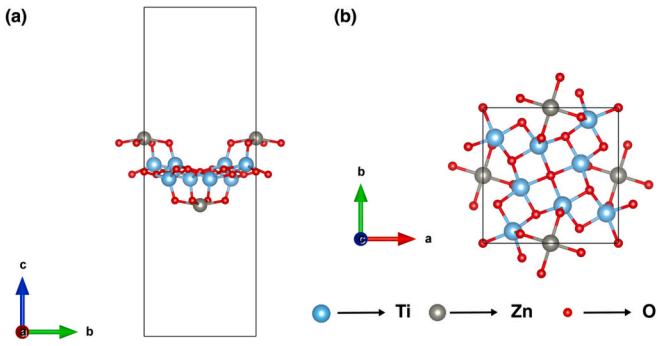


Fig. 1. The crystal structure of the Ti_4ZnO_9 material from (a) side and (b) top views.

Table 1
The optimized lattice parameters (a and c in Å), formation energy (E_{for} in eV/atom), elastic constants (C_{11}, C_{12}, and C_{66} in N/m), Young modulus (Y_{2D} in N/m), shear modulus (G_{2D} in N/m), and Poisson's ratio (ν) for the Ti_4ZnO_9 material.

a	c	E_{For}
8.68	25.49	−2.08
C_{11}	C_{12}	C_{66}
63.43	27.58	15.32
Y_{2D}	G_{2D}	ν
51.44	17.93	0.43

3. Results and discussions

3.1. Structural and stability considerations for Ti_4ZnO_9 material

The Ti_4ZnO_9 material has a square lattice as shown in Fig. 1 from both side and top views. This material was optimized and Table 1 lists the calculated lattice parameters, formation energy, elastic constant, Young's modulus, shear modulus and Poisson's ratio. As listed in Table 1, the formation energy calculated using the equation in [26] is negative which indicates the thermodynamic stability and experimental synthesizability. Furthermore, the exfoliation energy of the Ti_4ZnO_9 material is determined using **Eq. 1** [52,53] where E_{2D}, E_{bulk} and A correspond the total energy of the 2d layer, the total energy of the bulk phase and the cross-sectional area. E_{exf} is obtained as 162.04 meV/Å^2 which is higher from the exfoliation energy of the graphene as 20 meV/Å^2 [54,55] and lower than the required exfoliation energy criteria as 200 meV [56]. Therefore, Ti_4ZnO_9 material is found to be exfoliable from its bulk phase. In addition to the thermodynamic stability, the mechanical stability of the material under scrutiny was determined by calculating its elastic constants. In the configuration of a square lattice, the elastic constants required are designated as C_{11}, C_{12} and C_{66}. It is imperative that these constants must satisfy the Born stability criteria [57,58]. Accordingly, as indicated in Table 1, it is evident that the criteria are both met which are $C_{11} > 0$, $C_{66} > 0$ and $C_{11} > |C_{12}|$ [57,58]. It has thus been determined that the material is both mechanically and thermodynamically stable. The Young's modulus is a material's characteristics for resistance to being stretched and the material has a moderate Young's modulus value. The shear modulus is a material's characteristics for resistance to shear stress and the material again has a low shear modulus. The Poisson's ratio is a material's characteristics that indicates

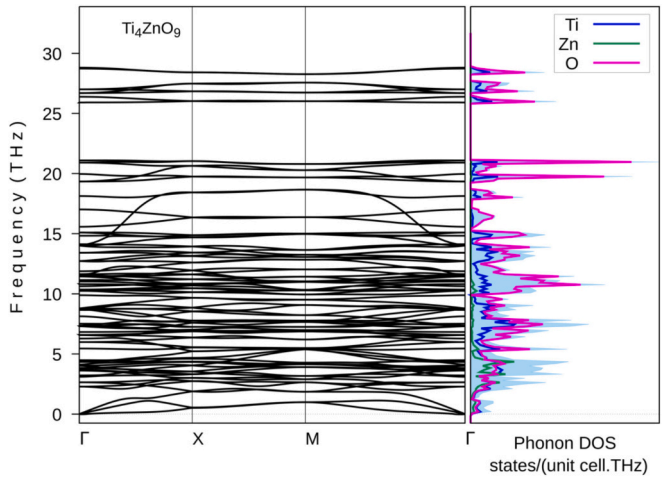


Fig. 2. Phonon dispersion curves and phonon DOS for the Ti_4ZnO_9 material.

the contraction in the perpendicular in-plane direction when it is stretched along one axis and this material has a high Poisson's ratio.

$$E_{exf} = (E_{2D} - E_{bulk})/A \quad (1)$$

The dynamical stability of the Ti_4ZnO_9 monolayer was evaluated using the finite displacement method within a $3 \times 3 \times 1$ supercell. The phonon dispersion curve as shown in Fig. 2, demonstrates no imaginary frequency. This observation indicates the dynamical stability of the Ti_4ZnO_9 monolayer. Moreover, the phonon density of states (DOS) was examined alongside the phonon dispersion curves, and projections were made onto atomic species. Projections indicate that oxygen atoms primarily contribute to high-frequency vibrational modes, while titanium and zinc atoms are predominantly present in the low- and mid-frequency ranges. The distribution under consideration is indicative of the lighter atomic mass of oxygen. The absence of imaginary modes within the Brillouin zone reveals the dynamic stability of the Ti_4ZnO_9 material, in addition to its thermodynamic and mechanical stability. Following the determination of the formation energy and the mechanical and dynamic stability of the material, the thermodynamic stability of Ti_4ZnO_9 was obtained by means of ab initio molecular dynamics (AIMD) calculations. To this end, machine learning force fields were utilized to speed up the AIMD calculations. **Fig. S1** illustrates the Bayesian error of the MLFF and the root mean square error (RMSE) of the forces for the Ti_4ZnO_9 material. As demonstrated in the figure, both the Bayesian error and the root mean square error (RMSE) value of the forces are minimal, indicating that the model has been adequately trained and is appropriate for precise AIMD calculations. Fig. 3 shows the total energy and temperature changes over 10,000 fs during AIMD calculations for the Ti_4ZnO_9 material. As demonstrated, both the total energy and temperature

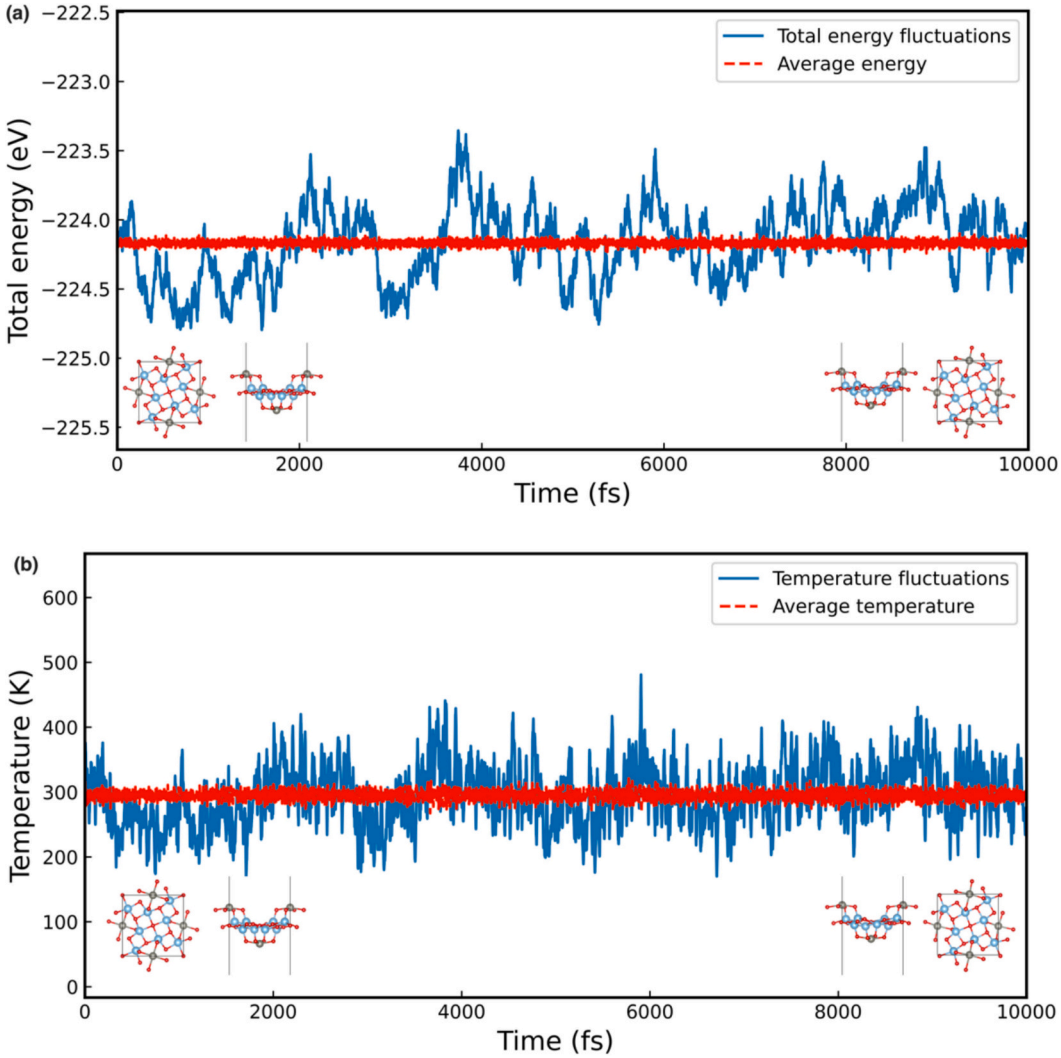


Fig. 3. (a) Total energy and (b) temperature fluctuations during AIMD simulations for the Ti_4ZnO_9 material.

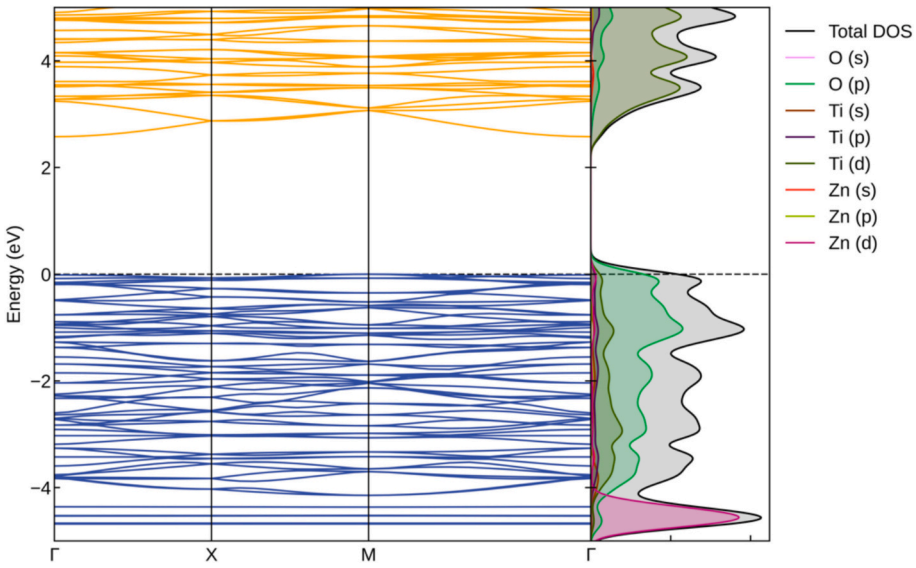


Fig. 4. Electronic band structure and DOS plots for the Ti_4ZnO_9 material.

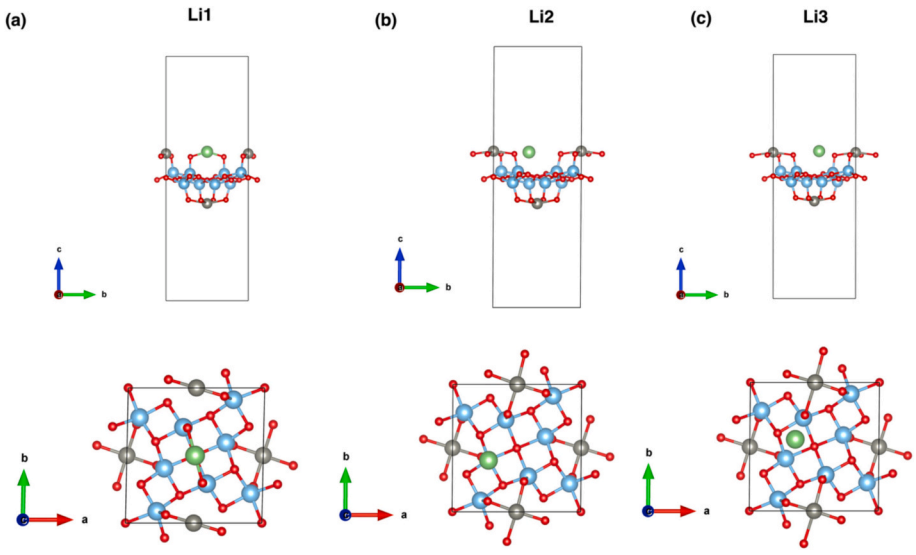


Fig. 5. Side and top views of (a) Li1, (b) Li2, and (c) Li3 decoration positions. (Li atoms are in green color.) (For interpretation of the references to color in this figure legend, the reader is referred to the web version of this article.)

demonstrate minimal fluctuations, thereby confirming the thermodynamic stability of the material at 300 K. The initial and final crystal structures are displayed in Fig. 3, and no significant changes are observed in this structure. The AIMD studies confirm the thermodynamic stability of the Ti_4ZnO_9 material, which also exhibits mechanical and dynamic stability.

After these stability considerations, the electronic band structure was determined for the Ti_4ZnO_9 material as shown in Fig. 4 along with the partial density of states (PDOS). As can be seen from the figure, there is a gap between the valence and conduction bands called band gap as 2.58 eV. This band gap value was obtained using the GGA-PBE method which is well-known with the underestimation of the band gaps in the literature. Despite the utilization of HSE or DFT + U methods to precisely estimate the band gap, it can be concluded that this material is an insulator, given that its band gap will exceed 2.5 eV. The PDOS plot reveals that the d states of Ti atoms contribute more to the conduction band while the p states of O atoms and the d states of Zn atoms contribute more to the valence band.

Table 2
The binding energy (E_{bind} in eV) and the distance between the Li atom and the Ti_4ZnO_9 material (d in Å).

Decoration	E_{bind}	d
Li1	−1.58	2.17
Li2	−0.52	1.89
Li3	−0.95	2.07

3.2. *Li decoration for Ti_4ZnO_9 material*

The metal decoration enhances the hydrogen storage capacities of the 2D materials. Therefore, the Li atom was chosen for the metal decoration of the Ti_4ZnO_9 material. Fig. 5 shows the different locations of the Li decoration on the Ti_4ZnO_9 material labeled as Li1, Li2, and Li3. The Li1 decoration is at the top of the O atom that is in the middle of the lattice. The Li2 decoration is at the top of the Ti atom. The Li3 decoration is at the middle of the square where the Ti and O atoms form. Each

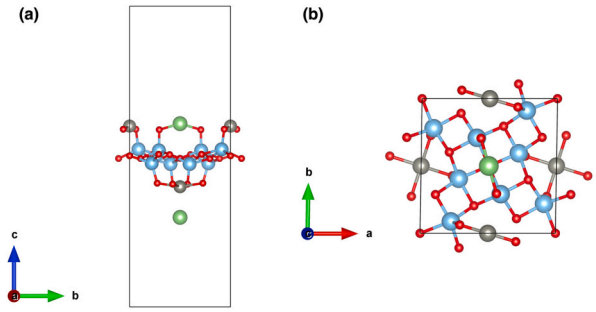


Fig. 6. (a) Side and (b) top views of two-sided Li1 decoration. (Li atoms are in green color.) (For interpretation of the references to color in this figure legend, the reader is referred to the web version of this article.)

decoration was optimized and the binding energies of these decorations were calculated using Eq. 2 [26]. Table 2 lists the calculated binding energies and the distance between the Li atom and the Ti_4ZnO_9 material. According to the table, the Li1 decoration has the lowest binding energy that reveals the energetic stability of this decoration position. Furthermore, the Li1 decoration has the highest distance between the Li atom and the Ti_4ZnO_9 material. For the hydrogen storage studies, the Li1 decoration was further investigated.

$$E_{bind} = E_{Li/Ti_4ZnO_9} - \left(E_{Ti_4ZnO_9} + E_{Li}\right) \quad (2)$$

Li1 decoration was to be the subject of further study in order to facilitate the development of hydrogen storage applications for this material. However, given the existence of extant literature on two-sided storage, two-sided decoration was applied to the Li1 decoration as illustrated in Fig. 6. Optimization of the two-sided Li1 decoration was undertaken to calculate the binding energy, which is found to be energetically stable with −0.62 eV binding energy value. The separation between the Li atoms and the Ti_4ZnO_9 material is determined to be 2.17 Å and 2.60 Å for the top and bottom Li atoms, respectively. As a result, this two-sided decoration was also considered for the hydrogen storage applications, as well.

The thermodynamic stabilities for the Li1 and two-sided Li1 decorated Ti_4ZnO_9 material were studied and Fig. 7 and Fig. 8 show the total energy and temperature changes. As demonstrated, both the total energy and temperature demonstrate minimal fluctuations, thereby confirming the thermodynamic stabilities of these decorations at 300 K. The initial and final crystal structures are displayed in Fig. 7 and Fig. 8, and no significant changes are observed for these decorations The AIMD studies confirm the thermodynamic stability of the Li1 and two-sided Li1 decorated Ti_4ZnO_9 material. In addition, **Fig. S2** and **Fig. S3** illustrate the Bayesian error of the MLFF and the root mean square error (RMSE) of the forces the Li1 and two-sided Li1 decorated Ti_4ZnO_9 material. As demonstrated in the figures, both the Bayesian error and the root mean

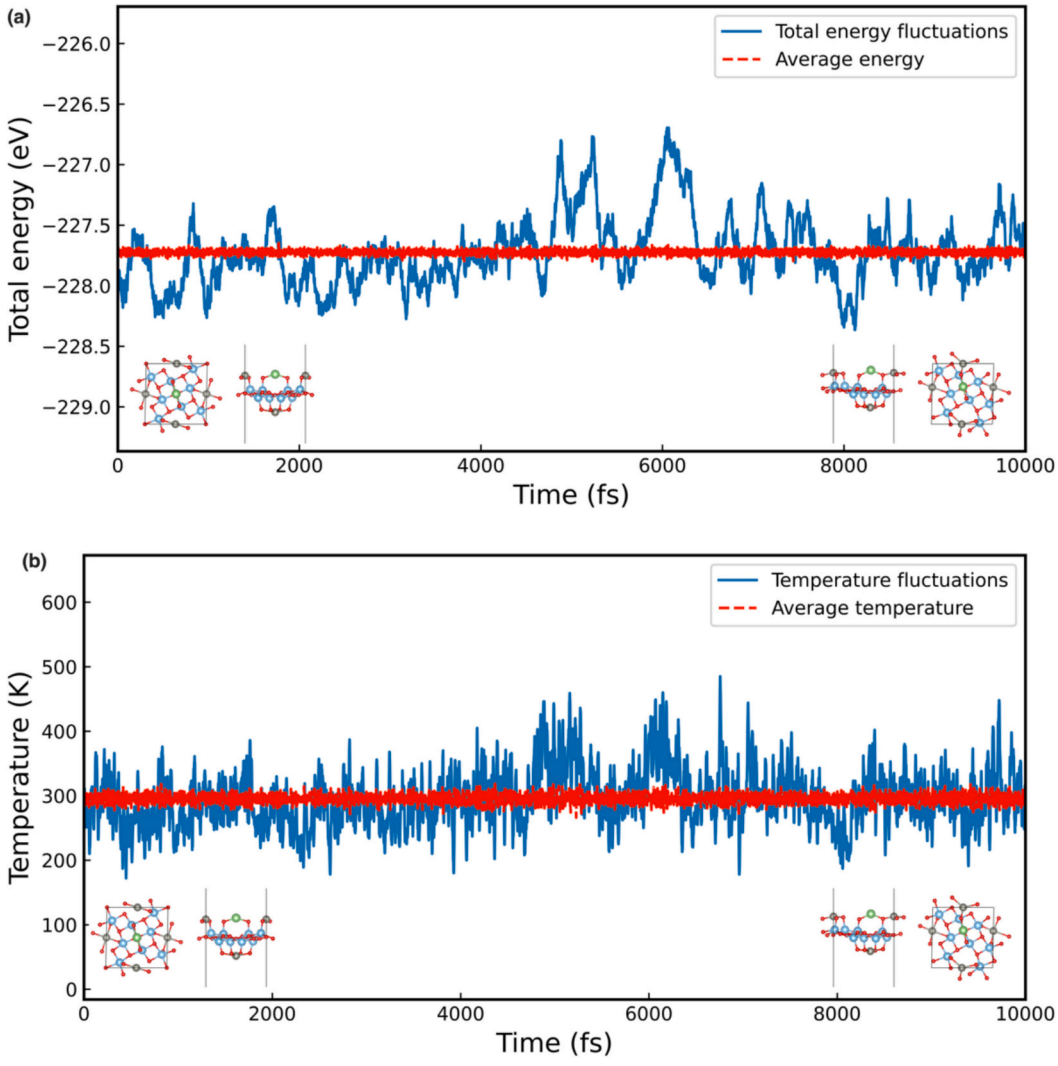


Fig. 7. (a) Total energy and (b) temperature fluctuations during AIMD simulations for the Li1 decorated Ti_4ZnO_9 material.

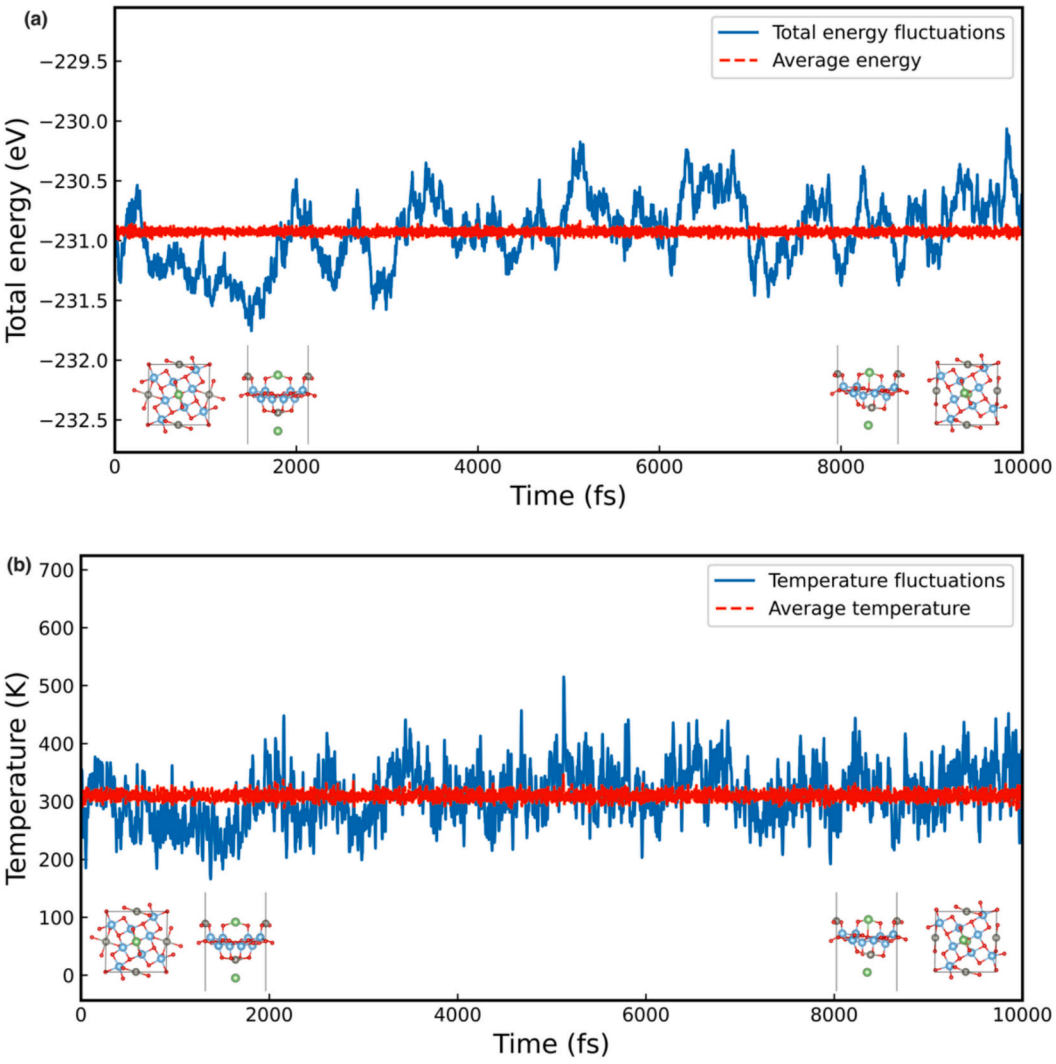


Fig. 8. (a) Total energy and (b) temperature fluctuations during AIMD simulations for the two-sided Li1 decorated Ti_4ZnO_9 material.

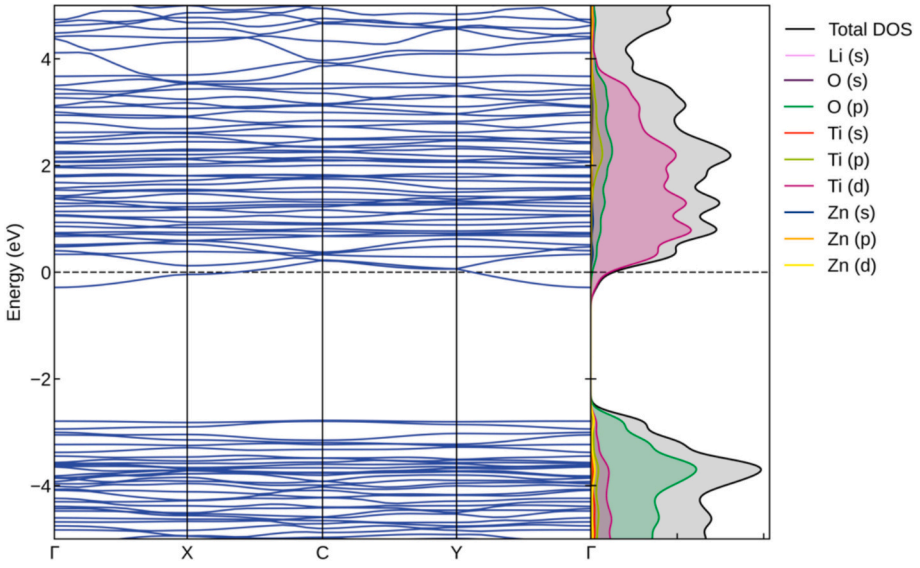


Fig. 9. Electronic band structure and DOS plots for the Li1 decorated Ti_4ZnO_9 materials.

square error (RMSE) value of the forces are minimal, indicating that the model has been adequately trained and is appropriate for precise AIMD

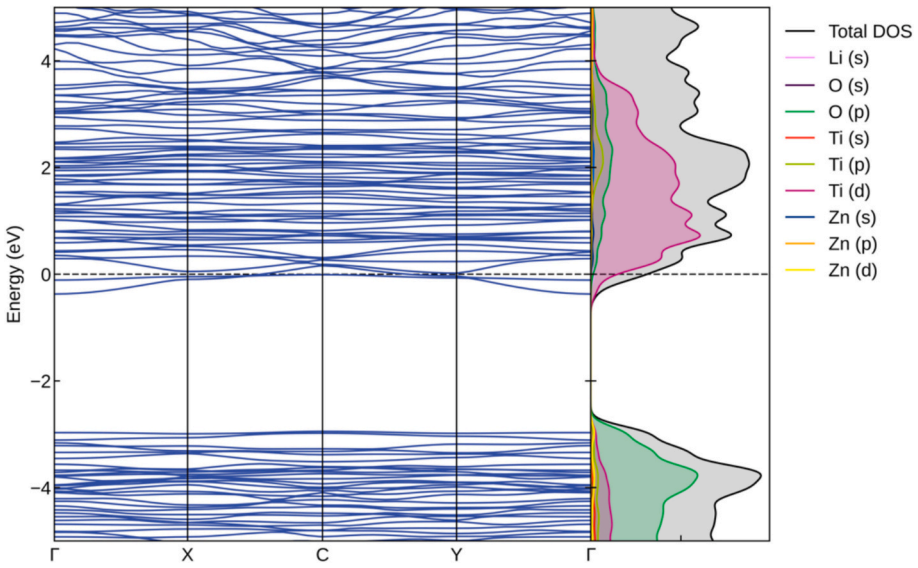


Fig. 10. Electronic band structure and DOS plots for the two-sided Li1 decorated Ti_4ZnO_9 materials.

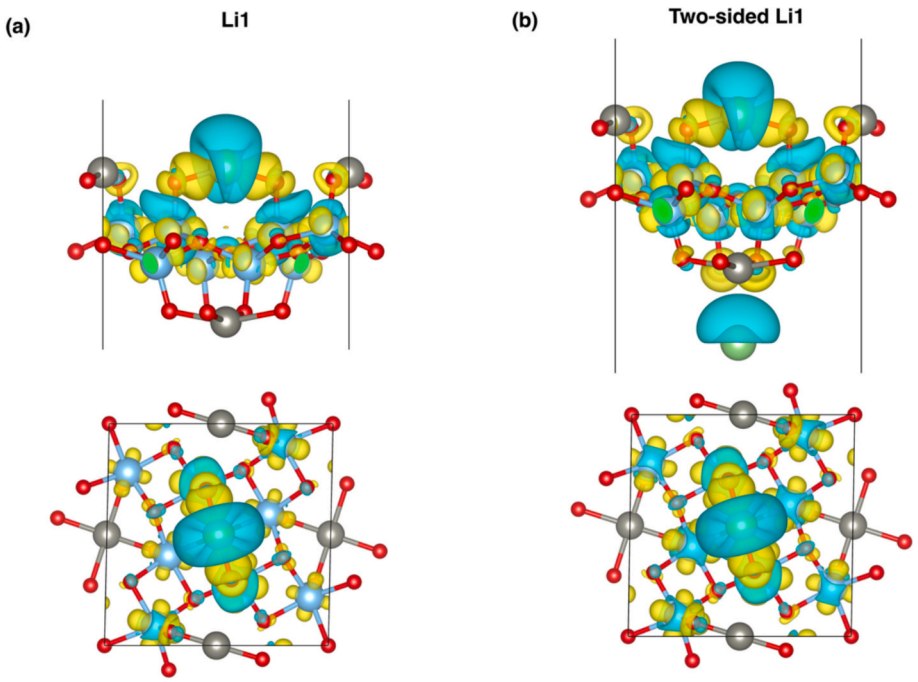


Fig. 11. Charge Density Difference visualizations for the (a) Li1 decorated and (b) two-sided Li1 decorated Ti_4ZnO_9 materials for side and top views (isosurface level = 0.0017 e/Å^3).

calculations.

The Li1 decorated and two-sided Li1 decorated Ti_4ZnO_9 materials were further investigated for their electronic properties and charge density difference analysis. Fig. 9 and Fig. 10 show the electronic band structures and DOS plots for these systems. As can be seen from the figures, these systems turn to metallic character after the Li decorations. In addition, the most contributions come from the d-states of Ti atoms for the conduction band and p states of O atoms for the valence band. The charge density difference plots for the one-sided and two-sided Li-decorated Ti_4ZnO_9 systems are presented in Fig. 11. For this purpose, Eq. 3 is used where ρ_{Li/Ti_4ZnO_9}, $\rho_{Ti_4ZnO_9}$, and ρ_{Li} represent the charge densities of the Li decorated Ti_4ZnO_9, Ti_4ZnO_9 and Li, respectively. In these images, blue areas show the regions where there are fewer electrons, and yellow areas show the regions where there are more electrons. Charge transfer is driven by their binding interaction, as indicated by a clear charge redistribution at the interface between the Li atoms and the Ti_4ZnO_9 surface. Specifically, electrons are found on the surface oxygen atoms of Ti_4ZnO_9, while there are fewer electrons around the Li atoms. This suggests that Li gives electrons to the surface and that Ti_4ZnO_9 accepts them. To quantify this effect, a Bader charge analysis was performed. The results show a net charge transfer of approximately |0.88|e in the one-sided configuration and |1.36|e in the two-sided case. These results confirm that Li atoms effectively donate electrons to the Ti_4ZnO_9 surface and that stronger charge transfer occurs in the symmetric, two-sided configuration due to enhanced electrostatic interactions.

$$\Delta\rho = \rho_{Li/Ti_4ZnO_9} - \rho_{Ti_4ZnO_9} - \rho_{Li} \quad (3)$$

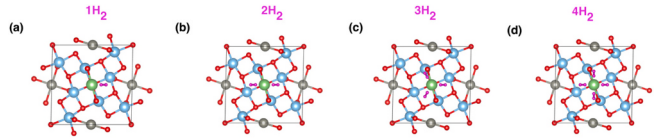


Fig. 12. Optimized hydrogen positions for (a) $1H_2$/Li1-Ti_4ZnO_9, (b) $2H_2$/Li1-Ti_4ZnO_9, (c) $3H_2$/Li1-Ti_4ZnO_9, and (d) $4H_2$/Li1-Ti_4ZnO_9 systems. (H atoms are in magenta color.) (For interpretation of the references to color in this figure legend, the reader is referred to the web version of this article.)

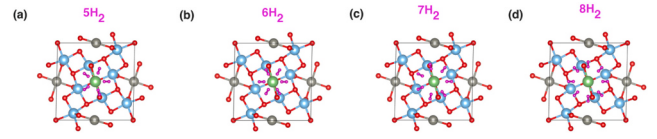


Fig. 13. Optimized hydrogen positions for (a) $5H_2$/Li1-Ti_4ZnO_9, (b) $6H_2$/Li1-Ti_4ZnO_9, (c) $7H_2$/Li1-Ti_4ZnO_9, and (d) $8H_2$/Li1-Ti_4ZnO_9 systems. (H atoms are in magenta color.) (For interpretation of the references to color in this figure legend, the reader is referred to the web version of this article.)

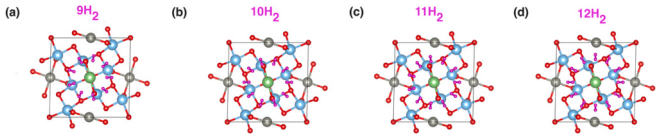


Fig. 14. Optimized hydrogen positions for (a) $9H_2$/Li1-Ti_4ZnO_9, (b) $10H_2$/Li1-Ti_4ZnO_9, (c) $11H_2$/Li1-Ti_4ZnO_9, and (d) $12H_2$/Li1-Ti_4ZnO_9 systems. (H atoms are in magenta color.) (For interpretation of the references to color in this figure legend, the reader is referred to the web version of this article.)

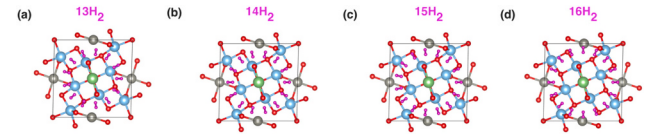


Fig. 15. Optimized hydrogen positions (a) $13H_2$/Li1-Ti_4ZnO_9, (b) $14H_2$/Li1-Ti_4ZnO_9, (c) $15H_2$/Li1-Ti_4ZnO_9, and (d) $16H_2$/Li1-Ti_4ZnO_9 systems. (H atoms are in magenta color.) (For interpretation of the references to color in this figure legend, the reader is referred to the web version of this article.)

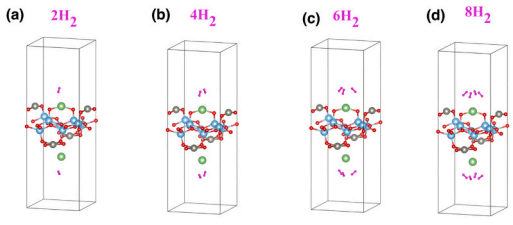


Fig. 16. Optimized hydrogen positions for (a) $2H_2$/two-sided Li1-Ti_4ZnO_9, (b) $4H_2$/two-sided Li1-Ti_4ZnO_9, (c) $6H_2$/two-sided Li1-Ti_4ZnO_9, and (d) $8H_2$/two-sided Li1-Ti_4ZnO_9 systems.

3.3. Hydrogen storage studies for the Li decorated Ti_4ZnO_9 material

The Li1 decorated and two-sided Li1 decorated Ti_4ZnO_9 materials were studied for the hydrogen storage applications. For this purpose, the initial coordinates of the hydrogen atoms were determined using the Cap-Like Initial Conditions for Hydrogens (CLICH) algorithm [40]. After the optimizations of the hydrogen adsorbed systems, the adsorption energy was calculated using Eq. 4 [26]. The adsorption energy is an essential consideration for hydrogen storage applications, with a range

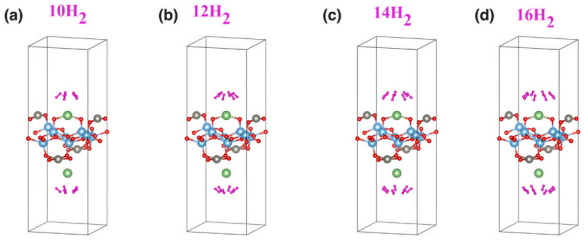


Fig. 17. Optimized hydrogen positions for (a) $10H_2$/two-sided Li1-Ti_4ZnO_9, (b) $12H_2$/two-sided Li1-Ti_4ZnO_9, (c) $14H_2$/two-sided Li1-Ti_4ZnO_9, and (d) $16H_2$/two-sided Li1-Ti_4ZnO_9 systems.

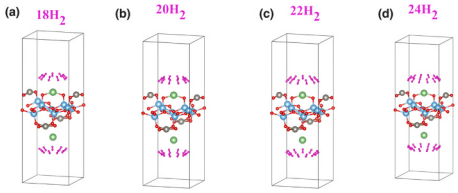


Fig. 18. Optimized hydrogen positions for (a) $18H_2$/two-sided Li1-Ti_4ZnO_9, (b) $20H_2$/two-sided Li1-Ti_4ZnO_9, (c) $22H_2$/two-sided Li1-Ti_4ZnO_9, and (d) $24H_2$/two-sided Li1-Ti_4ZnO_9 systems.

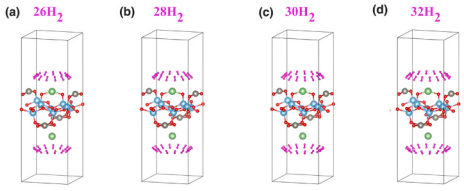


Fig. 19. Optimized hydrogen positions for (a) $26H_2$/two-sided Li1-Ti_4ZnO_9, (b) $28H_2$/two-sided Li1-Ti_4ZnO_9, (c) $30H_2$/two-sided Li1-Ti_4ZnO_9, and (d) $32H_2$/two-sided Li1-Ti_4ZnO_9 systems.

Table 3
The adsorption energy (E_{ads} in eV), the distance between a H atom and the Li atom ($d_{H\text{-}Li}$ in Å), and the average hydrogen bond length ($d_{H\text{-}H}$ in Å) for nH_2/Li1-Ti_4ZnO_9 systems.

nH_2	E_{ads}	$d_{H\text{-}Li}$		$d_{H\text{-}H}$
		Min	Max	
$1H_2$	0.82	2.79	2.94	0.74
$2H_2$	0.78	2.87	3.05	0.74
$3H_2$	0.78	2.96	3.24	0.74
$4H_2$	0.76	3.09	3.39	0.74
$5H_2$	0.73	3.27	3.56	0.74
$6H_2$	0.65	3.35	3.74	0.73
$7H_2$	0.66	3.67	3.85	0.73
$8H_2$	0.64	3.90	4.03	0.73
$9H_2$	0.53	4.04	4.15	0.73
$10H_2$	0.46	4.39	4.47	0.72
$11H_2$	0.34	4.33	4.53	0.72
$12H_2$	0.20	4.38	4.66	0.72

of 0.2–0.6 eV/H_2 being considered adequate for the practical hydrogen storage systems [59–61]. Figs. 12, 13, 14, 15 and Figs. 16, 17, 18, 19 show the hydrogen positions for nH_2/Li1-Ti_4ZnO_9 systems and nH_2/two-sided Li1-Ti_4ZnO_9 systems, respectively. The number of hydrogen molecules adsorb on the Li1 decorated and two-sided Li1 decorated Ti_4ZnO_9 materials were chosen as 16 and 32, respectively. Tables 3 and 4 list the hydrogen adsorption energy, the minimum and maximum distances for an H atom and a Li atom, and average H—H bond length for nH_2/Li1-Ti_4ZnO_9 systems and nH_2/two-sided Li1-Ti_4ZnO_9 systems,

Table 4
The adsorption energy (E_{ads} in eV), the distance between a H atom and a Li atom ($d_{H\text{-}Li}$ in Å), and the average hydrogen bond length ($d_{H\text{-}H}$ in Å) for nH_2/two-sided Li1-Ti_4ZnO_9 systems.

nH_2	E_{ads}	$d_{H\text{-}Li}$		$d_{H\text{-}H}$
		Min	Max	
$2H_2$	1.58	2.77	2.91	0.74
$4H_2$	1.18	2.88	3.05	0.74
$6H_2$	0.81	2.99	3.28	0.74
$8H_2$	0.84	3.11	3.40	0.74
$10H_2$	0.81	3.26	3.55	0.73
$12H_2$	0.74	3.23	3.91	0.73
$14H_2$	0.71	3.67	3.87	0.73
$16H_2$	0.62	3.86	4.04	0.73
$18H_2$	0.41	3.99	4.13	0.72
$20H_2$	0.31	4.17	4.30	0.72
$22H_2$	0.38	4.45	4.70	0.73
$24H_2$	0.14	4.59	4.72	0.72
$26H_2$	0.11	4.66	5.05	0.72

respectively. The Li1 decorated Ti_4ZnO_9 material can adsorb up to $12H_2$ molecules and for the $13H_2$, $14H_2$ and $15H_2$ cases the adsorption energy becomes negative that indicates the system is not adsorb hydrogen molecules and it is thermodynamically unstable. The hydrogen adsorb Li1 decorated Ti_4ZnO_9 material has suitable adsorption energies especially for $6H_2$ to 12 H_2 adsorptions. For the two-sided Li1 decorated Ti_4ZnO_9 material, the maximum adsorb number of H_2 is 26 and for the $28H_2$, $30H_2$, and $32H_2$ cases, the system has a negative adsorption energy that indicates the system is not adsorb hydrogen molecules and it is thermodynamically unstable. For the two-sided Li1 decorated Ti_4ZnO_9 material has suitable adsorption energies especially for $16H_2$ to 22 H_2 adsorptions. For both systems, when the number of adsorb hydrogen molecules increases, the adsorption energy decreases as can be seen from Fig. 20. The hydrogen bond lengths are listed in Tables 3 and 4 where there is a slight decrease when the number of adsorb hydrogen molecules increases. According to the literature, there are studies [40,62–66] that have this slight decrease for hydrogen bond lengths which aligns with the results of this study.

$$E_{ads} = -[E(nH_2/Li/Ti_4ZnO_9) - E(Li/Ti_4ZnO_9) - n \times E(H_2)]/n \quad (4)$$

The electronic band structures were studied for hydrogen adsorbed Li-decorated and two-sided Li1 decorated Ti_4ZnO_9 material. All hydrogen adsorbed systems show metallic character except for $24H_2$/Li1-Ti_4ZnO_9 and $26H_2$/Li1-Ti_4ZnO_9 systems. Figs. 21 and 22 shows the electronic band structures of the highest hydrogen adsorbed systems for the Li1-decorated and two-sided Li1 decorated Ti_4ZnO_9 material. As can be seen from the figures, the most contributions come from the d-states

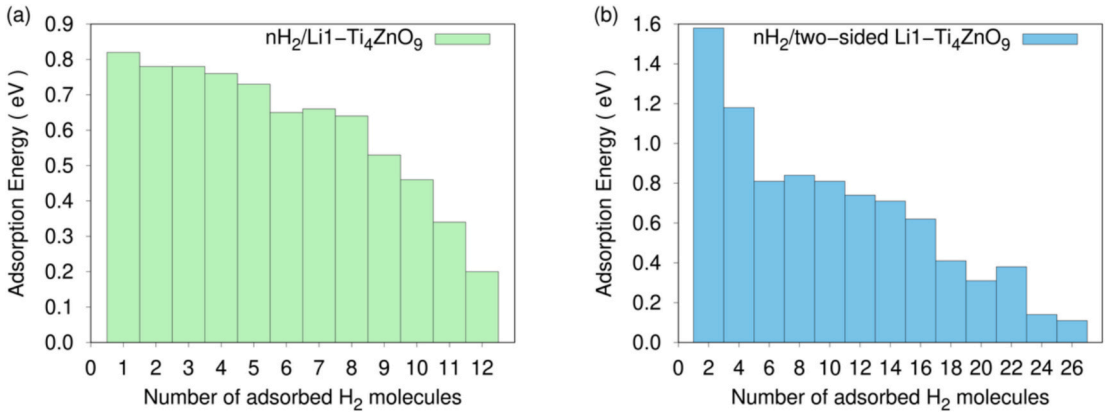


Fig. 20. Adsorption energy change as a function of number of adsorbed H_2 molecules for (a) nH_2/Li1-Ti_4ZnO_9 systems and (b) nH_2/two-sided Li1-Ti_4ZnO_9 systems.

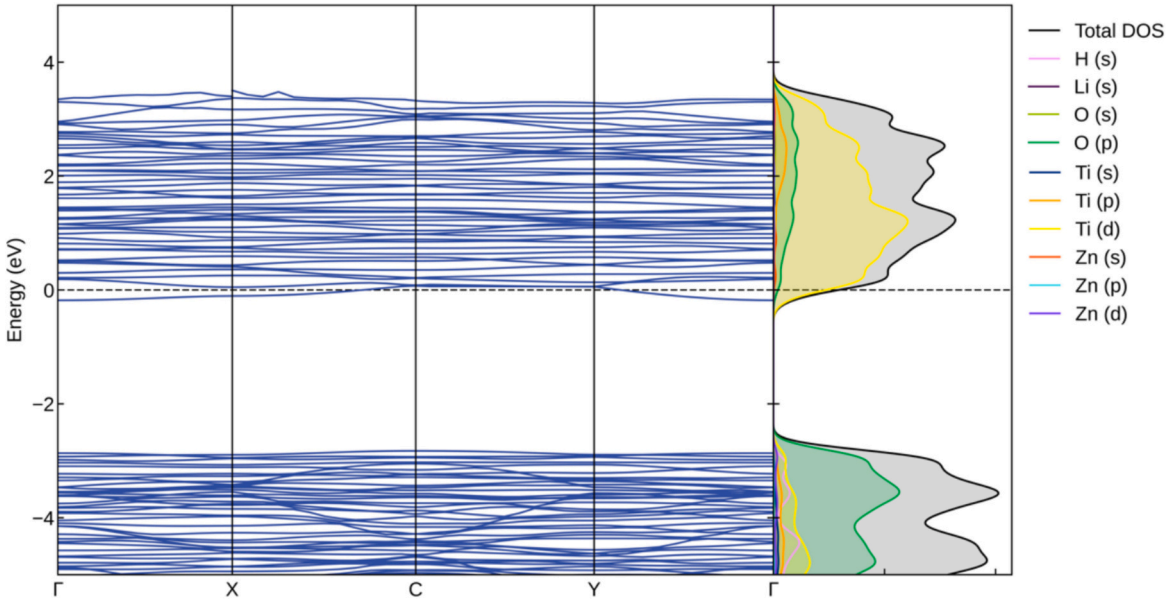


Fig. 21. Electronic band structure and DOS plots for the $12H_2$/Li1-Ti_4ZnO_9 system.

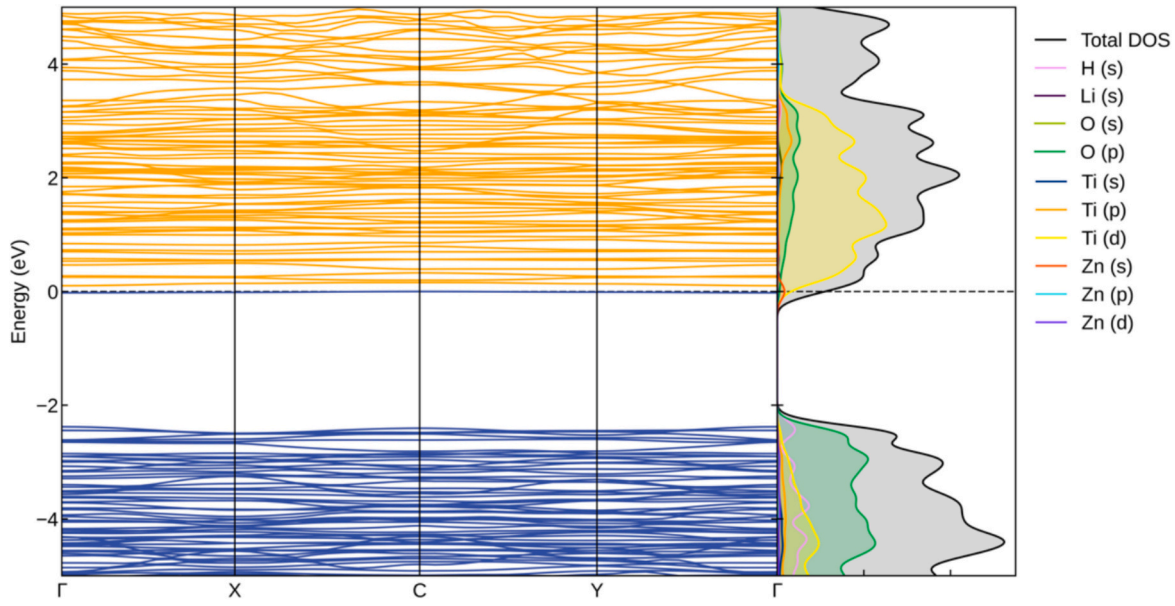


Fig. 22. Electronic band structure and DOS plots for the $26H_2$/two-sided Li1-Ti_4ZnO_9 system.

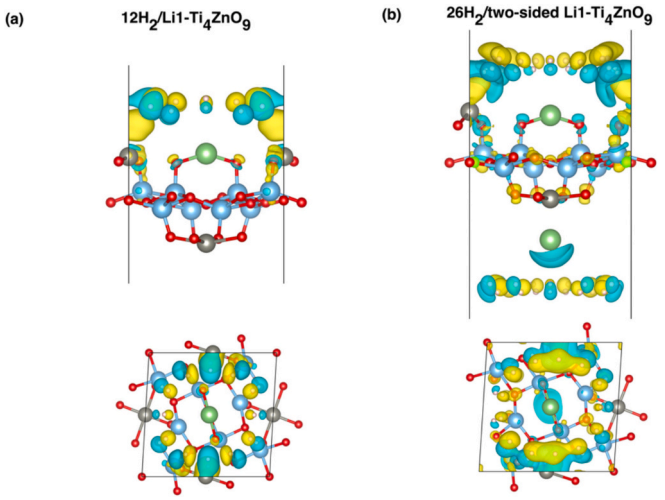


Fig. 23. Charge Density Difference visualizations for the (a) $12H_2$/Li1-Ti_4ZnO_9 and (b) $26H_2$/two-sided Li1-Ti_4ZnO_9 systems (isosurface level = 0.0002 e/Å^3).

of Ti atoms for the conduction band and p states of O atoms for the valence band for both systems. The $24H_2$/Li1-Ti_4ZnO_9 system has a 2.77 eV direct band gap that shows the semiconducting nature for this system. In contrast, the $26H_2$/Li1-Ti_4ZnO_9 system has a 0.1 eV indirect band gap that is very low. To elucidate the nature of the electronic interactions that occur during the process of hydrogen adsorption, the charge density difference plots are generated for the $12H_2$/Li1-Ti_4ZnO_9 and the $26H_2$/two-sided Li1-Ti_4ZnO_9 systems, as illustrated in Fig. 23. It can be observed that electron accumulation is evident in the vicinity of the adsorbed H_2 molecules in $12H_2$/Li1-Ti_4ZnO_9, coinciding with electron depletion in the immediate vicinity of the Li and Ti atoms of the Ti_4ZnO_9 material. This finding suggests the occurrence of charge transfer from the Li and Ti atoms to the adsorbed hydrogen, thereby implying the enhancement of physisorption. It is evident that for the $26H_2$/two-sided Li1-Ti_4ZnO_9 system, there is a more balanced charge redistribution, which is accompanied by significant electron accumulation, localized between the H_2 molecules and the adjacent Li and O sites. The spatial distribution of charge, as shown in the figure, indicates that Li atoms function as active sites, thereby facilitating H_2 adsorption. Furthermore, the performance of Bader charge analysis is of pivotal importance in elucidating the charge redistribution process that occurs as a consequence of hydrogen adsorption on Li-decorated Ti_4ZnO_9 material. In the one-sided $12H_2$ adsorbed configuration, the Li atom donates $+0.88|e|$, while in the two-sided $26H_2$ adsorbed system, this increases to $+1.50|e|$, indicating enhanced charge transfer under symmetric adsorption. In both cases, O atoms act as primary charge acceptors (−18.43 e and − 18.29 e, respectively), while Ti and Zn atoms exhibit comparable charges, indicative of their structural functionality. It has been demonstrated that hydrogen molecules exhibit minimal net charge transfer (−0.40 e and + 0.40 e for one-sided $12H_2$ case and − 0.49 e and + 0.36 e for two-sided $26H_2$ adsorbed systems, respectively) suggesting predominantly physisorption interactions. The findings, which demonstrate consistency with the charge density difference plots, indicate that Li decoration facilitates charge redistribution and plays a central role in modulating the strength of hydrogen adsorption on the Ti_4ZnO_9 material.

The thermodynamic stabilities for the maximum hydrogen adsorbed systems for the Li1 and two-sided Li1 decorated Ti_4ZnO_9 material were studied and **Fig. S4** and **Fig. S5** show the total energy and temperature changes. As demonstrated, both the total energy and temperature demonstrate minimal fluctuations, thereby confirming the thermodynamic stabilities of these hydrogen adsorbed systems at 300 K. The initial and final structures are displayed in the figures, and the changes in these systems are acceptable. The AIMD studies confirm the thermodynamic stability of the maximum hydrogen adsorbed systems for the Li1 and two-sided Li1 decorated Ti_4ZnO_9 material. In addition, **Fig. S4** and **Fig. S5** illustrate the Bayesian error of the MLFF and the root mean square error (RMSE) of the forces for the maximum hydrogen adsorbed systems for the Li1 and two-sided Li1 decorated Ti_4ZnO_9 material. As demonstrated in the figures, both the Bayesian error and the root mean square error (RMSE) value of the forces are minimal, indicating that the model has been adequately trained and is appropriate for precise AIMD calculations.

Determination of the gravimetric hydrogen storage capacity is of significant importance within the field of hydrogen storage research. The target set by the US Department of Energy in this regard is 5.5 wt% for 2025 [67]. The gravimetric hydrogen storage capacity was calculated using the **Eq. 5** [68,69] where n_{H_2}, m_{H_2} and $m_{nLi-Ti_4ZnO_9}$ are the number of adsorbed hydrogen molecules, the mass of hydrogen molecule, and the mass of Li decorated Ti_4ZnO_9 system. The results can be

Table 5
Gravimetric hydrogen storage capacities (C_{wt} %) and hydrogen desorption temperature (T_{des} in K) for nH_2/Li1-Ti_4ZnO_9 systems.

nH_2	C_{wt}	T_{des}
$1H_2$	0.25	611.35
$2H_2$	0.50	581.26
$3H_2$	0.74	581.03
$4H_2$	0.99	562.41
$5H_2$	1.23	543.87
$6H_2$	1.48	479.36
$7H_2$	1.72	488.05
$8H_2$	1.96	471.81
$9H_2$	2.20	395.09
$10H_2$	2.44	340.91
$11H_2$	2.67	249.65
$12H_2$	2.91	151.25

Table 6
Gravimetric hydrogen storage capacities (C_{wt} %) and hydrogen desorption temperature (T_{ides} in K) for nH_2/two-sided Li1-Ti_4ZnO_9 systems.

nH_2	C_{wt}	T_{ides}
$2H_2$	0.49	1176.61
$4H_2$	0.98	873.29
$6H_2$	1.46	600.54
$8H_2$	1.94	624.08
$10H_2$	2.42	603.97
$12H_2$	2.89	546.93
$14H_2$	3.35	524.29
$16H_2$	3.81	458.28
$18H_2$	4.27	302.43
$20H_2$	4.72	229.22
$22H_2$	5.17	284.16
$24H_2$	5.61	104.62
$26H_2$	6.05	85.24

found in Tables 5 and 6 for the nH_2/Li1-Ti_4ZnO_9 and nH_2/two-sided Li1-Ti_4ZnO_9 systems, respectively. Furthermore, for the purposes of clarity, the data presented in Tables 5 and 6 has been rendered into graphical form as Fig. 24. The results presented in the tables indicate that the gravimetric hydrogen storage capacity of the Li1 decorated and two-sided Li1 decorated Ti_4ZnO_9 materials have up to 2.91 wt% and 6.05 wt% gravimetric storage capacities, respectively. The two-sided case outperforms and also satisfies the US DOE targets.

$$C_{wt}\% = \frac{n_{H_2} m_{H_2}}{(n_{H_2} m_{H_2}) + m_{nLi-Ti_4ZnO_9}} \times 100 \quad (5)$$

Subsequent to the determination of the gravimetric hydrogen storage capacity, the hydrogen desorption temperature, a critical component in the hydrogen storage process, was obtained through using **Eq. 6** [70]. In this equation, E_{ads}, K_B, ΔS, R, and P denote adsorption energy, Boltzmann constant, the entropy change of the H_2 from gas phase to solid phase as 130 $J.mol^{-1}.K^{-1}$ [70], universal gas constant and equilibrium pressure as 1 atm. Tables 5 and 6 present the hydrogen desorption temperatures for the nH_2/Li1-Ti_4ZnO_9 and nH_2/two-sided Li1-Ti_4ZnO_9 systems, respectively. Upon evaluation of the values presented in the table, it is evident that the hydrogen release temperatures in the nH_2/Li1-Ti_4ZnO_9 and nH_2/two-sided Li1-Ti_4ZnO_9 systems decreases as the stored hydrogen increased. The lowest recorded hydrogen desorption temperature in the nH_2/Li1-Ti_4ZnO_9 and nH_2/two-sided Li1-Ti_4ZnO_9 systems are obtained for $12H_2$ and $26H_2$ cases.

$$T_{des} = \left(\frac{E_{ads}}{K_B}\right)\left(\frac{\Delta S}{R} - \ln(P)\right)^{-1} \quad (6)$$

A central finding of this study is the significant hydrogen storage capacity of the two-sided Li1-decorated Ti_4ZnO_9 system, which reaches a gravimetric density of 6.05 wt% with 26 adsorbed H_2 molecules. This result is highly promising as it successfully exceeds the 5.5 wt% target set by the US Department of Energy (DOE) for 2025. However, this maximum capacity must be analyzed in the context of its practical operational window. The average adsorption energy (E_{ads}) for the $26H_2$ system is 0.11 eV, which is below the ideal range of 0.2–0.6 eV required for efficient storage and release near ambient temperatures. This low adsorption energy directly results in a cryogenic desorption temperature (T_{des}) of 85.24 K. This suggests that while the material can hold a high volume of hydrogen, it would require significant cooling to achieve this maximum capacity, a challenge shared by many physisorption-based systems. Conversely, this study also highlights an important operational trade-off. For the $18H_2$/two-sided Li1 system, the E_{ads} is calculated to be 0.41 eV, falling perfectly within the ideal thermodynamic window. This configuration yields a desorption temperature of 302.43 K (approx. 29 °C), which is ideal for near-ambient applications. At this optimal energy, the material still delivers a high gravimetric capacity of 4.27 wt %. Therefore, the Li-decorated Ti_4ZnO_9 platform demonstrates significant versatility: it can either be optimized for maximum (cryogenic) capacity, exceeding DOE targets, or operated at ambient temperatures with a slightly lower, yet still substantial, reversible storage capacity. Furthermore, Table 7 presents the maximum number of adsorbed hydrogen molecules, adsorption energy, gravimetric storage capacity and hydrogen desorption temperature for some hydrogen storage systems. As presented in Table 7, the average adsorption energies for hydrogen storage systems range from 0.10 to 0.50 eV/H_2. The adsorption energies of the Li1 and double-sided Li1-decorated Ti_4ZnO_9 systems

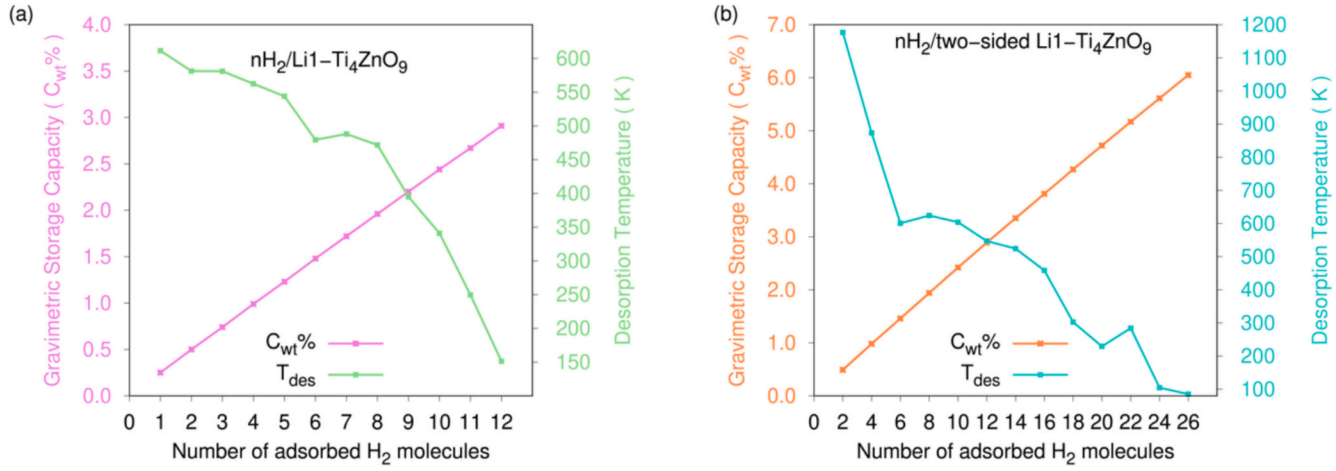


Fig. 24. Gravimetric storage capacity and desorption temperature as a function of number of adsorbed H_2 molecules for (a) nH_2/Li1-Ti_4ZnO_9 systems and (b) nH_2/two-sided Li1-Ti_4ZnO_9 systems.

Table 7
Maximum number of adsorbed H_2 molecules (n_{max}), adsorption energy ($|E_{ads}|$ in eV/H_2 molecule), gravimetric hydrogen storage capacity (C_{wt} %), and hydrogen desorption temperature (T_{des} in K) for some hydrogen storage system.

Systems	n_{max}	$\|E_{ads}\|$	C_{wt}	T_{des}	Reference
Li1-Ti_4ZnO_9	12	0.20	2.91	151.25	This study
two-sided Li1-Ti_4ZnO_9	26	0.11	6.05	85.24	This study
8Li@t-SiC	24	0.251	6.50	186.26	[71]
8Na@t-SiC	24	0.233	5.54	172.90	[71]
8 Mg@t-SiC	24	0.240	5.48	178.10	[71]
Na@B_7N_3	32	0.200	7.70	257.00	[72]
K@PHE-graphene	32	0.33	7.47	422.72	[65]
Li@β-NPD	48	0.15	19.80	188.17	[64]
Na@T-C_3N	16	0.11	10.63	140	[73]
Li@POG-$B_4C_2N_3$	10	0.19	8.35	245	[66]
Li@B_5N_3	13	0.209	7.70	257	[74]
V@biphenylene	5	0.510	7.52	596	[75]
16Li-BeN_4	64	0.25	12.21	200.9	[76]
8Li@GeC_5	24	0.22	7.62	281.10	[77]
Li@B14	40	0.212	11.2	271	[78]
OLi_3@Irida-graphene	12	0.19	10.00	273.74	[79]

examined in this study are found within this range. Furthermore, the gravimetric storage capacities of the systems under consideration range from 5 to 19 wt%, with the 6.05 wt% storage capacity obtained in this study representing a significant value. An examination of hydrogen release temperatures reveals a range of 85 to 400 K. The hydrogen release temperature at room temperature is of particular significance, and the 85.24 K obtained in this study is cryogenic. However, as previously referenced, the system with 18 H_2 attains a release temperature of 298.15 K at ambient temperature.

In addition to these investigations, the hydrogen adsorption and desorption at various temperature and pressure conditions are crucial. In order to obtain this, the thermodynamic analysis was performed using the grand canonical partition function Z as given in Eq. 7 [80–82].

$$Z = 1 + \sum_{i=1}^{n} e^{-\frac{\left(E_{ads}^{i} - \mu\right)}{k_B T}} \tag{7}$$

In Eq. 7, n is the maximum number of adsorbed H_2 molecules and E_{ads}^{i}, μ, and k_B corresponds to the adsorption energy of the nth adsorbed H_2 molecule, chemical potential of the gas phase of H_2 molecule and the Boltzmann constant. μ is a function of temperature and pressure and can be determined using Eq. 8 [80–82].

$$\mu = \Delta H + T\Delta S + k_B T \ln \frac{P}{P_0} \tag{8}$$

In Eq. 8, ΔH, ΔS, P, and P_0 corresponds to the enthalpy change, entropy change, pressure and atmospheric pressure, respectively. $\Delta H + T\Delta S$ can be obtained from the experimental database [83]. Eq. 9 was used to obtain number of stored H_2 molecules where N_0 is the maximum number of adsorbed H_2 molecules at 0 K [80–82].

$$N = N_0 \left[\frac{Z-1}{Z}\right] \tag{9}$$

Fig. 25 and Fig. 26 show the number of adsorbed H_2 molecules as a function of P and T for 12H_2/Li1-Ti_4ZnO_9 system and 26H_2/two-sided Li1-Ti_4ZnO_9 system, respectively. According to these figures, the H_2 molecules are adsorbed at low temperature and high-pressure conditions while the H_2 molecules are desorbed at high temperature and low-pressure conditions for both systems.

4. Conclusion

The present study systematically investigates the potential of a novel two-dimensional Ti_4ZnO_9 monolayer for hydrogen storage applications using first-principles density functional theory. The initial analysis confirmed that the pristine Ti_4ZnO_9 monolayer is an insulator that possesses thermodynamic, mechanical, and dynamic stability, indicating its experimental feasibility. To enhance hydrogen affinity, the material was decorated with Li atoms. The Li1 (top of O atom) position was identified as the most energetically stable decoration site. Li decoration was found to transition the material from an insulator to a metallic state, facilitating charge transfer. Bader charge analysis confirmed that Li atoms act as electron donors, polarizing the H_2

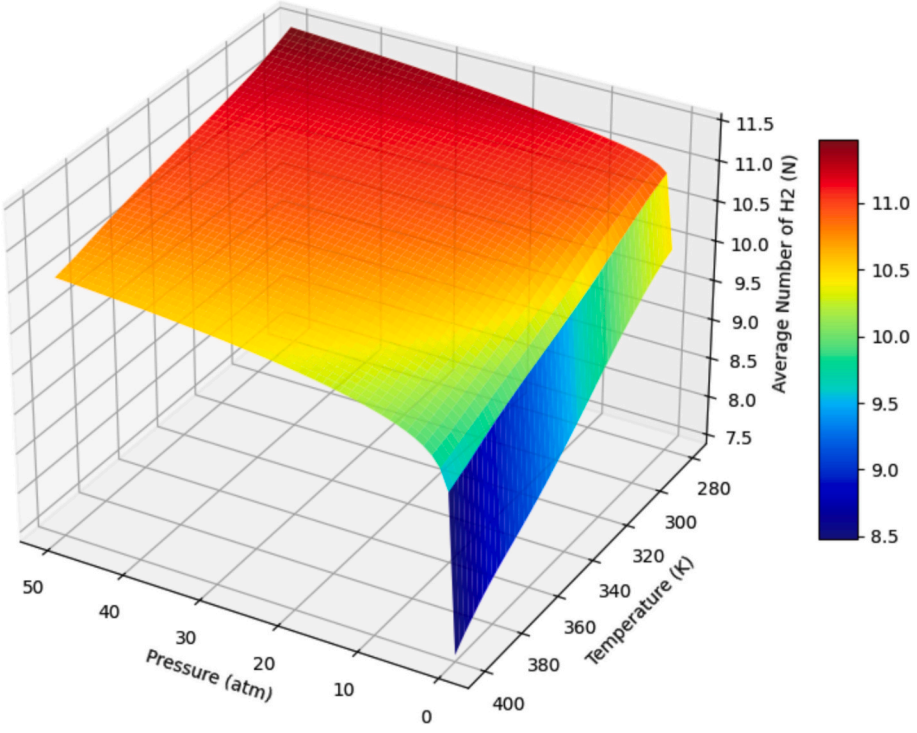


Fig. 25. Average number of H_2 molecules as a function of pressure and temperature for the 12H_2/Li1-Ti_4ZnO_9 system.

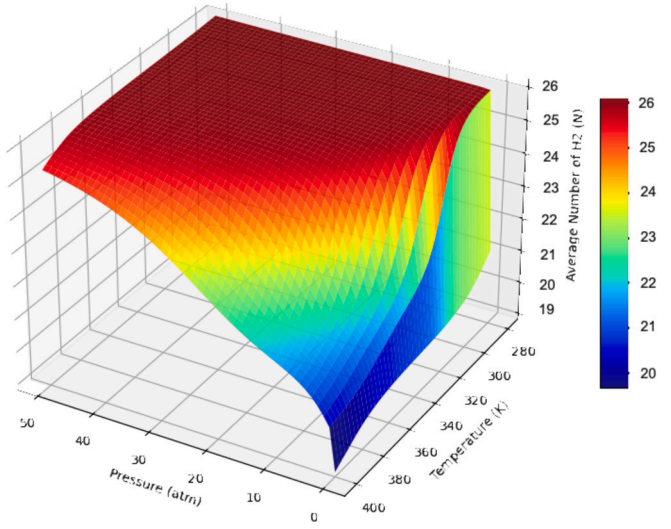


Fig. 26. Average number of H_2 molecules as a function of pressure and temperature for the $26H_2$/two-sided Li1-Ti_4ZnO_9 system.

molecules and enhancing the (physisorption) binding mechanism, which was further confirmed by charge density difference plots. The hydrogen storage performance of both single-sided and two-sided Li1-decorated systems was evaluated. The two-sided decorated system demonstrated superior performance, capable of adsorbing up to 26 H_2 molecules. This configuration achieves a maximum gravimetric storage capacity of 6.05 wt%, a value that successfully surpasses the US DOE 2025 target of 5.5 wt%. A critical trade-off between maximum capacity and operating temperature was identified. The 6.05 wt% capacity corresponds to a low adsorption energy (0.11 eV) and a cryogenic desorption temperature (85.24 K). However, the system also demonstrates excellent potential for near-ambient operation: at a loading of 18 H_2 molecules, it exhibits an ideal adsorption energy (0.41 eV), a practical desorption temperature of 302.43 K, and a high capacity of 4.27 wt %. These findings collectively establish Li-decorated Ti_4ZnO_9 as a highly promising and versatile new platform for solid-state hydrogen storage. Future works should focus on the experimental synthesis of this novel 2D material and validation of its hydrogen storage capabilities.

CRediT authorship contribution statement

Gokhan Surucu: Writing – review & editing, Validation, Supervision, Methodology, Funding acquisition, Conceptualization. **Cagri Karadeniz:** Writing – original draft, Investigation, Data curation. **Ozge Surucu:** Writing – original draft, Investigation, Conceptualization. **Aysenur Gencer:** Writing – original draft, Validation, Methodology, Conceptualization.

Declaration of Generative AI and AI-assisted technologies in the writing process

During the preparation of this work the authors used Google Gemini in order to enhance the language, clarity, and overall readability of the manuscript. After using this tool/service, the authors reviewed and edited the content as needed and take full responsibility for the content of the published article.

Declaration of competing interest

The authors declare that they have no known competing financial interests or personal relationships that could have appeared to influence the work reported in this paper.

Acknowledgments

As detailed in this study, the numerical calculations were performed using TRUBA resources at TUBITAK ULAKBIM, High Performance and Grid Computing Centre, and at Istanbul Technical University National Center for High-Performance Computing. This latter institution, which is known as ITU-UHEM, has a grant number for this project of 1024042025.

Appendix A. Supplementary data

Supplementary data to this article can be found online at https://doi.org/10.1016/j.est.2026.121209.

Data availability

Data will be made available on request.

References

[1] A.P. Pandey, V.K. Singh, A. Dixit, Recent Progress and Challenges in Hydrogen Storage Medium and Transportation for Boosting Hydrogen Economy, 2024, pp. 183–203, https://doi.org/10.1007/978-981-99-9009-2_15.
[2] H.T. Hwang, A. Varma, Hydrogen storage for fuel cell vehicles, Curr. Opin. Chem. Eng. 5 (2014) 42–48, https://doi.org/10.1016/j.coche.2014.04.004.
[3] F. Schüth, Challenges in hydrogen storage, Eur Phys J Spec Top 176 (2009) 155–166, https://doi.org/10.1140/epjst/e2009-01155-x.
[4] A. Salehabadi, M.I. Ahmad, N. Ismail, N. Morad, M. Enhessari, Solid-State Hydrogen Storage Materials, 2020, pp. 41–67, https://doi.org/10.1007/978-981-15-4906-9_4.
[5] R. P. Prachi, M. W. Mahesh, C. G. Aneesh, A review on solid state hydrogen storage material, Adv. Energy Power 4 (2016) 11–22, https://doi.org/10.13189/aep.2016.040202.
[6] T.K. Mandal, D.H. Gregory, Hydrogen storage materials: present scenarios and future directions, Annual Reports Section "A" (Inorganic Chemistry) 105 (2009) 21, https://doi.org/10.1039/b818951j.
[7] M. Jangir, N.S. Rawat, H. Kumar, Solid-State Materials for Hydrogen Storage, 2024, pp. 491–514, https://doi.org/10.1007/978-981-97-1339-4_20.
[8] X. Lin, J. Jia, P. Hubberstey, M. Schröder, N.R. Champness, Hydrogen storage in metal–organic frameworks, CrystEngComm 9 (2007) 438–448, https://doi.org/10.1039/B706207A.
[9] A. Razouk, M. EL Kassaoui, M. Boubkri, A. Benyoussef, O. Mounkachi, Enhanced hydrogenation properties of two-dimensional MgH2 by doping, vacancy-like defects and strain engineering: A theoretical study, Int. J. Hydrog. Energy 92 (2024) 1078–1090, https://doi.org/10.1016/J.IJHYDENE.2024.10.357.
[10] W. Osborn, T. Markmaitree, L.L. Shaw, R. Ren, J. Hu, J.H. Kwak, Z. Yang, Solid-state hydrogen storage: Storage capacity, thermodynamics, and kinetics, JOM 61 (2009) 45–51, https://doi.org/10.1007/s11837-009-0051-5.
[11] A. Hamaed, T.K.A. Hoang, M. Trudeau, D.M. Antonelli, Optimization of hydrogen storage capacity in silica-supported low valent Ti systems exploiting Kubas binding of hydrogen, J. Organomet. Chem. 694 (2009) 2793–2800, https://doi.org/10.1016/j.jorganchem.2009.02.034.
[12] A. Melicchio, P.F. Liguori, B. Russo, G. Golemme, Strategy for the enhancement of H2 uptake in porous materials containing TiO2, Int. J. Hydrog. Energy 41 (2016) 5733–5740, https://doi.org/10.1016/j.ijhydene.2016.02.050.
[13] X. Hu, B.O. Skadtchenko, M. Trudeau, D.M. Antonelli, Hydrogen storage in chemically reducible mesoporous and microporous Ti oxides, J. Am. Chem. Soc. 128 (2006) 11740–11741, https://doi.org/10.1021/ja0639766.
[14] H. Pan, J. Luo, H. Sun, Y. Feng, C. Poh, J. Lin, Hydrogen storage of ZnO and Mg doped ZnO nanowires, Nanotechnology 17 (2006) 2963–2967, https://doi.org/10.1088/0957-4484/17/12/023.
[15] Y. Zhang, X. Xue, T. He, H. Zhang, S. Zhang, J. Wang, A. Li, Y. Liu, A review on advances, strategies, and future perspectives of solid-state hydrogen storage materials, Sustainable Chemistry for Energy Materials 2 (2025) 100014, https://doi.org/10.1016/j.scenem.2025.100014.
[16] M.J.S. Spencer, I. Yarovsky, W. Wlodarski, K. Kalantar-zadeh, Interaction of hydrogen with zinc oxide nanorods: Why the spacing is important, Nanotechnology 22 (2011) 135704, https://doi.org/10.1088/0957-4484/22/13/135704.
[17] C. Cheng, A. Amini, C. Zhu, Z. Xu, H. Song, N. Wang, Enhanced photocatalytic performance of TiO2-ZnO hybrid nanostructures, Sci. Rep. 4 (2014) 4181, https://doi.org/10.1038/srep04181.
[18] M. Pelaez, N.T. Nolan, S.C. Pillai, M.K. Seery, P. Falaras, A.G. Kontos, P.S. M. Dunlop, J.W.J. Hamilton, J.A. Byrne, K. O'Shea, M.H. Entezari, D.D. Dionysiou, A review on the visible light active titanium dioxide photocatalysts for environmental applications, Appl. Catal. B 125 (2012) 331–349, https://doi.org/10.1016/j.apcatb.2012.05.036.
[19] M. Dincă, J.R. Long, Hydrogen storage in microporous metal–organic frameworks with exposed metal sites, Angew. Chem. Int. Ed. 47 (2008) 6766–6779, https://doi.org/10.1002/anie.200801163.

[20] A. Züttel, C. Nützenadel, P. Sudan, P. Mauron, C. Emmenegger, S. Rentsch, L. Schlapbach, A. Weidenkaff, T. Kiyobayashi, Hydrogen sorption by carbon nanotubes and other carbon nanostructures, J. Alloys Compd. 330–332 (2002) 676–682, https://doi.org/10.1016/S0925-8388(01)01659-0.

[21] T. Yildirim, S. Ciraci, Titanium-decorated carbon nanotubes as a potential high-capacity hydrogen storage medium, Phys. Rev. Lett. 94 (2005) 175501, https://doi.org/10.1103/PhysRevLett.94.175501.

[22] K. Gopalsamy, V. Subramanian, Hydrogen storage capacity of alkali and alkaline earth metal ions doped carbon based materials: A DFT study, Int. J. Hydrog. Energy 39 (2014) 2549–2559, https://doi.org/10.1016/j.ijhydene.2013.11.075.

[23] W. Zhou, J. Zhou, J. Shen, C. Ouyang, S. Shi, First-principles study of high-capacity hydrogen storage on graphene with Li atoms, J. Phys. Chem. Solids 73 (2012) 245–251, https://doi.org/10.1016/j.jpcs.2011.10.035.

[24] F. Wang, T. Zhang, X. Hou, W. Zhang, S. Tang, H. Sun, J. Zhang, Li-decorated porous graphene as a high-performance hydrogen storage material: A first-principles study, Int. J. Hydrog. Energy 42 (2017) 10099–10108, https://doi.org/10.1016/j.ijhydene.2017.01.121.

[25] D. Luo, X. Zhang, H. Chen, Stabilized Li-decoration and enhanced hydrogen storage on reduced graphene oxides, Int. J. Hydrog. Energy 44 (2019) 31192–31203, https://doi.org/10.1016/j.ijhydene.2019.09.183.

[26] A. Gencer, S. Aydin, O. Surucu, X. Wang, E. Deligoz, G. Surucu, Enhanced hydrogen storage of a functional material: Hf2CF2 MXene with Li decoration, Appl. Surf. Sci. 551 (2021) 149484, https://doi.org/10.1016/J.APSUSC.2021.149484.

[27] S. Mishra, S. Pakhira, S.I. Kundalwal, Tailoring hydrogen storage performance of heteroatoms-doped polycrystalline carbon nanotubes via Ti functionalization: A molecular dynamics study, Int. J. Hydrog. Energy 206 (2026) 153372, https://doi.org/10.1016/J.IJHYDENE.2026.153372.

[28] P. Kerdsombut, P. Latthiwan, N. Thatsami, P. Reunchan, A. Boonchun, T. Hussain, S. Pinitsoontorn, T. Kaewmaraya, Revealing the reversible hydrogen storage potential of light transition-metal decorated organic C5N monolayers, J. Energy Storage 143 (2026) 119608, https://doi.org/10.1016/J.EST.2025.119608.

[29] G. Kresse, J. Furthmüller, Efficiency of ab-initio total energy calculations for metals and semiconductors using a plane-wave basis set, Comput. Mater. Sci. 6 (1996) 15–50, https://doi.org/10.1016/0927-0256(96)00008-0.

[30] G. Kresse, J. Furthmüller, Efficient iterative schemes for *ab initio* total-energy calculations using a plane-wave basis set, Phys. Rev. B 54 (1996) 11169, https://doi.org/10.1103/PhysRevB.54.11169.

[31] J.P. Perdew, K. Burke, M. Ernzerhof, Generalized gradient approximation made simple, Phys. Rev. Lett. 77 (1996) 3865, https://doi.org/10.1103/PhysRevLett.77.3865.

[32] P.E. Blöchl, Projector augmented-wave method, Phys. Rev. B 50 (1994) 17953, https://doi.org/10.1103/PhysRevB.50.17953.

[33] G. Kresse, D. Joubert, From ultrasoft pseudopotentials to the projector augmented-wave method, Phys. Rev. B 59 (1999) 1758, https://doi.org/10.1103/PhysRevB.59.1758.

[34] J.D. Pack, H.J. Monkhorst, "Special points for Brillouin-zone integrations"—A reply, Phys. Rev. B 16 (1977) 1748, https://doi.org/10.1103/PhysRevB.16.1748.

[35] A. Togo, L. Chaput, T. Tadano, I. Tanaka, Implementation strategies in phonopy and phono3py, J. Phys. Condens. Matter 35 (2023) 353001, https://doi.org/10.1088/1361-648X/ACD831.

[36] A. Togo, First-principles phonon calculations with Phonopy and Phono3py, J. Phys. Soc. Jpn. 92 (2022) 012001-1-012001-21, https://doi.org/10.7566/JPSJ.92.012001.

[37] S. Grimme, J. Antony, S. Ehrlich, H. Krieg, A consistent and accurate ab initio parametrization of density functional dispersion correction (DFT-D) for the 94 elements H-Pu, J. Chem. Phys. 132 (2010), https://doi.org/10.1063/1.3382344.

[38] S.M. Kastuar, C.E. Ekuma, Z.L. Liu, Efficient prediction of temperature-dependent elastic and mechanical properties of 2D materials, Sci. Rep. 2022 (12:1 12) (2022) 1–8, https://doi.org/10.1038/s41598-022-07819-8.

[39] Z.L. Liu, C.E. Ekuma, W.Q. Li, J.Q. Yang, X.J. Li, ElasTool: An automated toolkit for elastic constants calculation, Comput. Phys. Commun. 270 (2022) 108180, https://doi.org/10.1016/J.CPC.2021.108180.

[40] S. Aydin, M. Şimşek, The enhancement of hydrogen storage capacity in Li, Na and Mg-decorated BC3 graphene by CLICH and RICH algorithms, Int. J. Hydrog. Energy 44 (2019) 7354–7370, https://doi.org/10.1016/J.IJHYDENE.2019.01.222.

[41] H.T. Chen, Y.M. Choi, M. Liu, M.C. Lin, A theoretical study of surface reduction mechanisms of CeO2(111) and (110) by H2, ChemPhysChem 8 (2007) 849–855, https://doi.org/10.1002/CPHC.200600598.

[42] K. Momma, F. Izumi, VESTA 3 for three-dimensional visualization of crystal, volumetric and morphology data, Urn:Issn:0021–8898, J. Appl. Crystallogr. 44 (2011) 1272–1276, https://doi.org/10.1107/S0021889811038970.

[43] A.M. Ganose, A.J. Jackson, D.O. Scanlon, Sumo: Command-line tools for plotting and analysis of periodic *ab initio* calculations, J. Open Source Softw. 3 (2018) 717, https://doi.org/10.21105/JOSS.00717.

[44] W. Tang, E. Sanville, G. Henkelman, A grid-based Bader analysis algorithm without lattice bias, J. Phys. Condens. Matter 21 (2009) 084204, https://doi.org/10.1088/0953-8984/21/8/084204.

[45] R.F.W. Bader, Atoms in Molecules: A Quantum Theory, Oxford University Press, 1990, p. 438. https://global.oup.com/academic/product/atoms-in-molecules-9780198558651. (Accessed 1 August 2025).

[46] D.S. Lemons, A. Gythiel, Paul Langevin''s 1908 paper "On the Theory of Brownian Motion" ["Sur la théorie du mouvement brownien," C. R. Acad. Sci. (Paris) 146, 530–533 (1908)], Am. J. Phys. 65 (1997) 1079–1081, https://doi.org/10.1119/1.18725.

[47] D.J. Evans, Computer "'experiment"' for nonlinear thermodynamics of Couette flow, J. Chem. Phys. 78 (1983) 3297–3302, https://doi.org/10.1063/1.445195.

[48] R. Jinnouchi, F. Karsai, G. Kresse, On-the-fly machine learning force field generation: Application to melting points, Phys. Rev. B 100 (2019) 014105, https://doi.org/10.1103/PhysRevB.100.014105.

[49] R. Jinnouchi, F. Karsai, C. Verdi, R. Asahi, G. Kresse, Descriptors representing two- and three-body atomic distributions and their effects on the accuracy of machine-learned inter-atomic potentials, J. Chem. Phys. 152 (2020), https://doi.org/10.1063/5.0009491.

[50] J. Behler, M. Parrinello, Generalized neural-network representation of high-dimensional potential-energy surfaces, Phys. Rev. Lett. 98 (2007) 146401, https://doi.org/10.1103/PhysRevLett.98.146401.

[51] C.M. Bishop, Pattern Recognition and Machine Learning 2016, Springer., 2006.

[52] Z. Wang, J. Jiang, H. Tang, H. Guo, W. Wang, Z. Zhuo, N. Lu, Phosphorene-like SiP3 monolayer as a promising anode material for alkali metal ion batteries, J. Energy Storage 141 (2026) 119223, https://doi.org/10.1016/J.EST.2025.119223.

[53] T. Barnowsky, A.V. Krasheninnikov, R. Friedrich, T. Barnowsky, A. V. Krasheninnikov, R. Friedrich, A new group of 2D non-van der Waals materials with ultra low exfoliation energies, Adv Electron Mater 9 (2023) 2201112, https://doi.org/10.1002/AELM.202201112.

[54] T. Björkman, A. Gulans, A.V. Krasheninnikov, R.M. Nieminen, Van der Waals bonding in layered compounds from advanced density-functional first-principles calculations, Phys. Rev. Lett. 108 (2012) 235502, https://doi.org/10.1103/PhysRevLett.108.235502.

[55] R. Zacharia, H. Ulbricht, T. Hertel, Interlayer cohesive energy of graphite from thermal desorption of polyaromatic hydrocarbons, Phys. Rev. B 69 (2004) 155406, https://doi.org/10.1103/PhysRevB.69.155406.

[56] K. Choudhary, I. Kalish, R. Beams, F. Tavazza, High-throughput identification and characterization of two-dimensional materials using density functional theory, Sci. Rep. 7 (1 7) (2017) 5179, https://doi.org/10.1038/s41598-017-05402-0, 2017.

[57] V. Wang, G. Tang, Y.C. Liu, R.T. Wang, H. Mizuseki, Y. Kawazoe, J. Nara, W. T. Geng, High-throughput computational screening of two-dimensional semiconductors, J. Phys. Chem. Lett. 13 (2022) 11581–11594, https://doi.org/10.1021/ACS.JPCLETT.2C02972.

[58] M. Born, K. Huang, Dynamical Theory Of Crystal Lattices, Dynamical theory of crystal lattices, 1996, https://doi.org/10.1093/OSO/9780192670083.001.0001.

[59] Y.H. Kim, Y. Zhao, A. Williamson, M.J. Heben, S.B. Zhang, Nondissociative adsorption of H2 molecules in light-element-doped fullerenes, Phys. Rev. Lett. 96 (2006) 016102, https://doi.org/10.1103/PHYSREVLETT.96.016102.

[60] X. Jin, P. Qi, H. Yang, Y. Zhang, J. Li, H. Chen, Enhanced hydrogen adsorption on Li-coated B12C6N6, J. Chem. Phys. 145 (2016), https://doi.org/10.1063/1.4964394.

[61] S.R. Naqvi, T. Hussain, W. Luo, R. Ahuja, Metallized siligraphene nanosheets (SiC7) as high capacity hydrogen storage materials, Nano Res. 11 (2018) 3802–3813, https://doi.org/10.1007/S12274-017-1954-Z.

[62] Q. Yin, G. Bi, R. Wang, Z. Zhao, K. Ma, High-capacity hydrogen storage in Li-decorated defective penta-BN2: A DFT-D2 study, Int. J. Hydrog. Energy 48 (2023) 26288–26300, https://doi.org/10.1016/J.IJHYDENE.2023.03.309.

[63] Q. Wang, H. Sun, Q. Li, X. Yang, W. Chen, J. Yan, Y. Lyu, G. Yan, H. Zhao, Z. Meng, Z. Yang, Y. Wang, Enhanced hydrogen storage in K and Na decorated DHP-graphene monolayer: DFT and GCMC study, Chem. Phys. Lett. 865 (2025) 141932, https://doi.org/10.1016/J.CPLETT.2025.141932.

[64] Y.Z. Abdullahi, J.A.S. Laranjeira, J.R. Sambrano, β-Naphthyldiene: A novel multifunctional 2D material for energy storage applications, J. Energy Storage 122 (2025) 116631, https://doi.org/10.1016/J.EST.2025.116631.

[65] J.A.S. Laranjeira, N.F. Martins, L. Ye, J.R. Sambrano, X. Chen, Hydrogen storage engineering in PHE-graphene monolayer via potassium (K) decoration, Int. J. Hydrog. Energy 123 (2025) 139–149, https://doi.org/10.1016/J.IJHYDENE.2025.03.288.

[66] X. Chen, J. Wang, N.F. Martins, J.R. Sambrano, J.A.S. Laranjeira, Penta-Octa B4C2N3: A new 2D material for high-performance energy applications, Langmuir 41 (2025) 5477–5487, https://doi.org/10.1021/ACS.LANGMUIR.4C05139.

[67] DOE Technical Targets for Onboard Hydrogen Storage for Light-Duty Vehicles | Department of Energy, (n.d.). https://www.energy.gov/eere/fuelcells/doe-technical-targets-onboard-hydrogen-storage-light-duty-vehicles (accessed September 10, 2025).

[68] M.S. Zyane, H. Rghioui, A. Achahbar, O. Boujibar, F.T. Van, M. Zanouni, A. Marjaoui, A novel lithium-decorated GeC5 monolayer for promising hydrogen storage: A DFT study, Int. J. Hydrog. Energy 114 (2025) 131–141, https://doi.org/10.1016/J.IJHYDENE.2025.03.022.

[69] Z. Duan, S. Shi, C. Yao, J. Hu, X. Liu, K. Diao, Y. Liu, Reversible hydrogen storage of Mg-decorated C7N3: A study based on density functional theory, J. Energy Storage 127 (2025) 116673, https://doi.org/10.1016/J.EST.2025.116673.

[70] A. Benaddi, A. Elomrani, N. Khossossi, M. Maymoun, S. Oukahou, A. Etrini, A. Hasnaoui, First-principles prediction of new stable 2D orthorhombic (o)-B2CN and o-B2C2 materials for hydrogen storage applications via lithium decoration, Int. J. Hydrog. Energy 127 (2025) 116–126, https://doi.org/10.1016/J.IJHYDENE.2025.03.389.

[71] M. EL Kassaoui, M. Houmad, M. Lakhal, A. Benyoussef, A. El Kenz, M. Loulidi, Hydrogen storage in lithium, sodium and magnesium-decorated on tetragonal silicon carbide, Int. J. Hydrog. Energy 46 (2021) 24190–24201, https://doi.org/10.1016/J.IJHYDENE.2021.04.183.

[72] Z. Liu, X. Chen, Y. Liao, L. Zhang, J.A.S. Laranjeira, First-principles insights of na-decorated B7N5 monolayer for advanced hydrogen storage, Surf. Interfaces 58 (2025) 105802, https://doi.org/10.1016/J.SURFIN.2025.105802.

[73] J.A.S. Laranjeira, N.F. Martins, B.D. Aparicio-Huacarpuma, K.A.L. Lima, L. A. Ribeiro, J.R. Sambrano, Two-dimensional T-C3N functionalized with sodium: A

promising platform for solid-state hydrogen storage, Phys. B Condens. Matter 719 (2025) 417945, https://doi.org/10.1016/J.PHYSB.2025.417945.
[74] X. Chen, L. Zhang, H. Jia, P. Gao, Computational investigation of a reversible energy storage medium in g-B5N3 decorated by lithium, Langmuir 40 (2024) 11582–11589, https://doi.org/10.1021/ACS.LANGMUIR.4C00779.
[75] P. Mane, S.P. Kaur, M. Singh, A. Kundu, B. Chakraborty, Superior hydrogen storage capacity of vanadium decorated biphenylene (Bi+V): A DFT study, Int. J. Hydrog. Energy 48 (2023) 28076–28090, https://doi.org/10.1016/J.IJHYDENE.2023.04.033.
[76] M. Rafique, Y. Shuai, B.A. Kalwar, B.G. Lougou, A. Ghorbal, B. Wang, L. Li, P. Łapka, D.S. Takou, Investigations on Lithium decorated light weight BeN4 for reversible and enhanced hydrogen storage; an ab-initio molecular dynamic (AIMD) study, Renew. Energy 240 (2025) 122217, https://doi.org/10.1016/J.RENENE.2024.122217.
[77] M.S. Zyane, H. Rghioui, A. Achahbar, O. Boujibar, F.T. Van, M. Zanouni, A. Marjaoui, A novel lithium-decorated GeC5 monolayer for promising hydrogen storage: A DFT study, Int. J. Hydrog. Energy 114 (2025) 131–141, https://doi.org/10.1016/J.IJHYDENE.2025.03.022.
[78] X. Chen, L. Zhang, Z. Dai, Y. Liu, J. Li, F. Long, R. Wu, F. Zhai, P. Gao, Computational investigation of Li-decorated B14 as a room temperature reversible energy storage medium, Int. J. Hydrog. Energy 101 (2025) 1439–1447, https://doi.org/10.1016/J.IJHYDENE.2024.12.415.
[79] J.A.S. Laranjeira, W. Elaggoune, N.F. Martins, X. Chen, J.R. Sambrano, OLi3-decorated irida-graphene for high-capacity hydrogen storage: A first-principles study, J. Phys. Chem. Solids 207 (2025) 112951, https://doi.org/10.1016/J.JPCS.2025.112951.
[80] L.J. Ma, J. Xu, J. Wang, J. Jia, H.S. Wu, Hydrogen adsorption on metal-decorated BN atom-pair substituted biphenylene network: A DFT investigation, J. Energy Storage 114 (2025) 115889, https://doi.org/10.1016/J.EST.2025.115889.
[81] T. Kaewmaraya, N. Thatsami, P. Tangpakonsab, R. Kinkla, K. Kotmool, C. Menendez, K.F. Aguey-Zinsou, T. Hussain, Ultrahigh hydrogen storage using metal-decorated defected biphenylene, Appl. Surf. Sci. 629 (2023) 157391, https://doi.org/10.1016/J.APSUSC.2023.157391.
[82] R. Rahimi, M. Solimannejad, DFT investigation of reversible hydrogen storage employing Li-decorated δ-5 boron monolayers, Mater. Sci. Semicond. Process. 199 (2025) 109818, https://doi.org/10.1016/J.MSSP.2025.109818.
[83] A. Hashmi, M.U. Farooq, I. Khan, J. Son, J. Hong, Ultra-high capacity hydrogen storage in a Li decorated two-dimensional C2N layer, J. Mater. Chem. A Mater. 5 (2017) 2821–2828, https://doi.org/10.1039/C6TA08924K.